PCCP

PAPER

View Article Online
View Journal | View Issue

Check for updates

Cite this: *Phys. Chem. Chem. Phys.*, 2019, **21**, 8489

Substitutional disorder: structure and ion dynamics of the argyrodites Li_6PS_5Cl, Li_6PS_5Br and Li_6PS_5I†

I. Hanghofer,*[a] M. Brinek,[a] S. L. Eisbacher,[a] B. Bitschnau,[b] M. Volck,[c] V. Hennige,[c] I. Hanzu,[ad] D. Rettenwander[a] and H. M. R. Wilkening*[ad]

Received 2nd February 2019,
Accepted 27th March 2019

DOI: 10.1039/c9cp00664h

rsc.li/pccp

For the development of safe and long-lasting lithium-ion batteries we need electrolytes with excellent ionic transport properties. Argyrodite-type Li_6PS_5X (X: Cl, Br, I) belongs to a family of such a class of materials offering ionic conductivities, at least if Li_6PS_5Br and Li_6PS_5Cl are considered, in the mS cm^{-1} range at room temperature. Although already tested as ceramic electrolytes in battery cells, a comprehensive picture about the ion dynamics is still missing. While Li_6PS_5Br and Li_6PS_5Cl show an exceptionally high Li ion conductivity, that of Li_6PS_5I with its polarizable I anions is by some orders of magnitude lower. This astonishing effect has not been satisfactorily understood so far. Studying the ion dynamics over a broad time and length scale is expected to help shed light on this aspect. Here, we used broadband impedance spectroscopy and ^{7}Li NMR relaxation measurements and show that very fast local Li ion exchange processes are taking place in all three compounds. Most importantly, the diffusion-induced NMR spin–lattice relaxation in Li_6PS_5I is almost identical to that of its relatives. Considering the substitutional disorder effects in Li_6PS_5X (X = Br, Cl), we conclude that in structurally ordered Li_6PS_5I the important inter-cage jump processes are switched off, hindering the ions from taking part in long-range ion transport.

1 Introduction

Energy from renewable sources can be stored in various ways. Considering electrochemical storage, Li-based batteries offer high energy densities combined with a high degree of design flexibility.[1–3] In particular, batteries using Li$^+$ as an ionic charge carrier are an emerging option to power electric vehicles.[1–7] Such batteries may, however, suffer from flammable fluorinated liquid electrolytes conventionally used in these energy storage systems. Next-generation Li batteries with, *e.g.*, metallic Li anodes and equipped with solid electrolytes have aroused great interest.[8–12] Devices with non-flammable ceramic electrolytes are anticipated to benefit from increased safety as they easily withstand higher temperatures. Thus, such systems are less sensitive to thermal runaway.

To take full advantage of all-solid-state Li (or Na) batteries, electrolytes with exceptionally high ionic conductivities are needed.[8–15] In the past, only a few ceramics were available fulfilling this requirement.[16,17] This lack of suitable materials prevented any commercialization on a large scale.[18,19] Ideal candidates should (i) show room-temperature ionic conductivities with values comparable to those of liquids, (ii) be chemically stable over a sufficiently wide temperature range and (iii) possess a sufficiently high electrochemical stability over a large potential window.[10,11] For battery applications, the conductivity of a ceramic material should reach a value of 10^{-3} S cm^{-1} at room temperature.[10,14]

Over the last years several classes of materials have been presented whose members show very high conductivities. These materials include sulfides, such as $Li_7P_3S_{11}$ and $Li_{10}GeP_2S_{12}$, oxides including garnets, such as $Li_7La_3Zr_2O_{12}$, or phosphates based on the NASICON structure.[8–15,20–26] Although the ionic bulk conductivities of oxides and phosphates can reach very high values, the materials may suffer from high grain boundary (g.b.) resistances.[27] For the softer sulfides the difference between the bulk and g.b. conductivities[28] is expected to be much lower. Of course, Li-bearing sulfides or thiophosphates are sensitive to air and moisture, thus requiring careful handling and adequate processing. As an example, the Ge-containing thiophosphate $Li_{10}GeP_2S_{12}$ (LGPS),[13] which initiated the renaissance to consider

---

[a] Christian Doppler Laboratory for Lithium Batteries and Institute for Chemistry and Technology of Materials, Graz University of Technology (NAWI Graz), Stremayrgasse 9, 8010 Graz, Austria. E-mail: isabel.hanghofer@tugraz.at, wilkening@tugraz.at; Fax: +43 316 873 32332; Tel: +43 316 873 32330

[b] Institute of Physical and Theoretical Chemistry, Graz University of Technology, Stremayrgasse 9, 8010 Graz, Austria

[c] AVL List GmbH, 8020 Graz, Austria

[d] Alistore-ERI European Research Institute, 33 rue Saint Leu, 80039 Amiens, France

† Electronic supplementary information (ESI) available: Rietveld refinements and structural data, further NMR data. See DOI: 10.1039/c9cp00664h

sulfide-based systems as candidates for solid electrolytes, is characterised by an ionic conductivity of 12 mS cm^{-1}. Meanwhile the expensive element Ge has been replaced by cheaper and naturally abundant materials.[29] The electrochemical stability of LGPS-based systems needs, however, to be improved.[30]

Besides LGPS, Deiseroth and co-workers introduced Li-containing argyrodite-type Li_6PS_5X (X = Cl, Br, I).[31] The crystal structure is shown in Fig. 1; the possible Li exchange processes are illustrated as well. As an example, the ionic conductivity of Li_6PS_5Br and Li_6PS_5Cl is reported to range from 10^{-3} S cm^{-1} to 10^{-2} S cm^{-1} depending on the preparation technique, which influences the type and number of defects as well as the overall morphology.[32,33] Thus, the ionic conductivity of Li-argyrodites is only slightly smaller than that of the LGPS family. Lower costs make this family of electrolytes highly attractive for application in all-solid-state batteries.[31,34]

In 2008 Deiseroth *et al.* reported the solid-state synthesis of Li_6PS_5X (X = Cl, Br, I) and characterised the local and long-range structure by X-ray diffraction and NMR.[31] Three years later Rao *et al.* discussed the synthesis of the lithium argyrodite *via* ball milling.[35] Rayavarapu *et al.* showed that the disorder in both the lithium distribution over the available cation sites and the disorder in the S^{2-}/Cl^- and S^{2-}/Br^- sublattices promotes lithium ion conductivity.[36] This view has further been supported by bond-valence calculations.[37]

Over the last years a number of studies have been carried out to measure the ionic conductivities of the Li_6PS_5X family by using standard impedance measurements.[31–40] The overall goal, not only for Li_6PS_5X, is to relate macroscopic application relevant properties to crystal chemical and morphological properties. So far, the results reported have rarely been related to the length-scale specific properties of the measuring technique applied. The ionic conductivities for Li_6PS_5X vary from 10^{-7} S cm^{-1} to 10^{-2} S cm^{-1}, while the highest values are found for X = Cl, Br. The corresponding activation energies reported, either experimentally probed or calculated, take values from 0.11 eV to 0.57 eV.[31–40] Astonishingly, the I-compound Li_6PS_5I shows the lowest conductivity. According to the strategy of substitutional disorder, size mismatch and polarizability of the halogen anion one could have expected the opposite trend. Replacing S by a larger and more polarizable anion such as I, as compared to the small and unpolarizable Li cation, is expected to cause lattice distortions which on their part lead to a broader distribution of slightly inequivalent Li sites in the Li sublattice. Without any strong site preference of the Li ions they are expected to jump quickly between the local minima of such a heterogeneous, *i.e.*, non-uniformly shaped, potential landscape. Such a situation, sometimes also connected to geometric frustration, is very similar to F diffusion in the recently investigated system $(Ba,Ca)F_2$,[41,42] Li diffusion in $Li_7La_3Zr_2O_{12}$ oxides[43] and Na diffusion in some *closo*-borates.[44] While this situation might be the origin for the high conductivity in Li_6PS_5Br and Li_6PS_5Cl, for the I analogue it seems to incompletely describe the real situation as for Li_6PS_5I relatively low ion conductivities are reported.

In an elegant way, Kraft *et al.*[34] tried to establish a connection between the stiffness (or polarizability) of the anion sublattice in Li_6PS_5X and the macroscopic ionic transport properties. They used impedance spectroscopy and ultrasonic speed of sound measurements to collect information on activation energies and the pre-factors governing the underlying Arrhenius equation. They reported that soft lattices, as is the case for Li_6PS_5I, lead to smaller Arrhenius pre-factors than obtained for Li_6PS_5Cl and Li_6PS_5Br. This decrease in pre-factor, which might originate from a change of the migration entropy or attempt frequencies, has been used to explain the low (overall) ion conductivity in Li_6PS_5I.

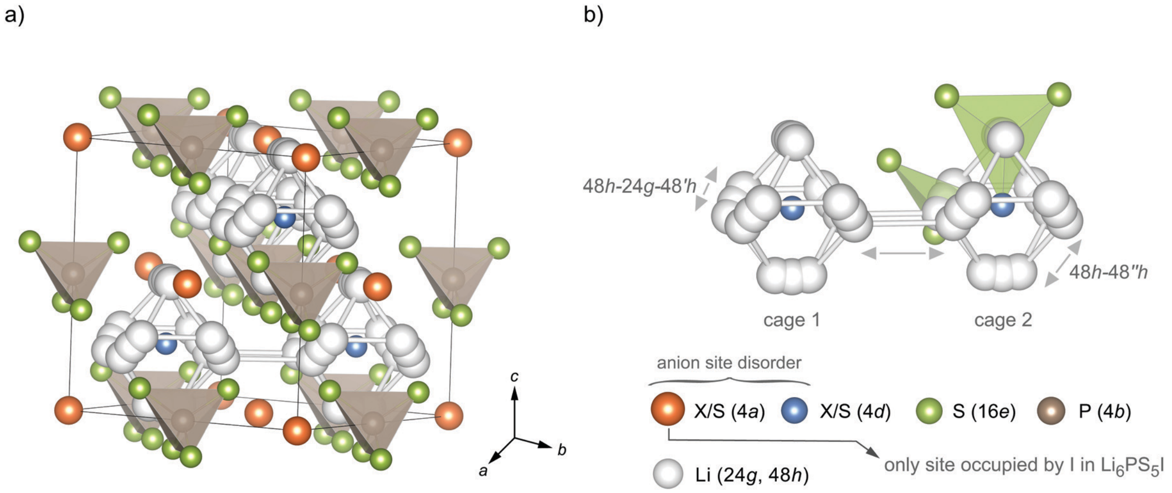

Fig. 1 (a) Crystal structure of argyrodite-type Li_6PS_5X (X = Cl, Br, I). In a perfect ordered structure, a cubic lattice is formed with PS_4^{3-} tetrahedra and Li ions being arranged octahedrally. Some of the S^{2-} (4d) anions are placed in the middle of the Li octahedra; the anions on 4a form a face centred cubic lattice. (b) The two different lithium positions (24g, 48h) form an octahedral arrangement in which three different jump processes can occur: (i) strictly localised jumps between the Li positions 48h–24g–48h′; (ii) intracage jumps (48h–48h″) and (iii) so-called intercage jumps $48h_1$–$48h_2$ between two neighbouring cages 1 and 2. The latter jump process forms interconnected diffusion pathways being responsible for 3D long-range ion transport. Site disorder on the anion positions 4a and 4d, which is absent for Li_6PS_5I, is expected to influence the Li ion diffusivity significantly.

Here, we employed impedance and NMR spectroscopy to shed more light on the effect seen for Li_6PS_5I. The important structural differences between the three argyrodites have to be taken into account to explain the significant changes in ionic conductivities, pre-factors and activation energies. For this purpose we have not only looked at the monosubstituted compounds like Li_6PS_5X, but also at samples with two or three different anions such as $Li_6PS_5Cl_{0.5}Br_{0.5}$ or $Li_6PS_5Cl_{1/3}Br_{1/3}I_{1/3}$. The non-substituted compound Li_7PS_6 served as a reference material. Importantly, complementary techniques which are sensitive to ion dynamics on different length-scales and time-scales are used to fully characterise the transport properties. We will show that, on a short-range length scale, the Li ions in Li_6PS_5I are as rapid as in the Br and Cl analogues. Obviously, the ordered S^{2-}/I^- sublattice, as compared to the disordered situation for Li_6PS_5Cl and Li_6PS_5Br, is responsible for a more regular potential landscape with a higher degree of site preference for the Li ions. As a consequence, we assume that intercage jump processes in Li_6PS_5I occur less frequently. These processes are, however, needed to establish rapid long-range ion dynamics in the iodide.

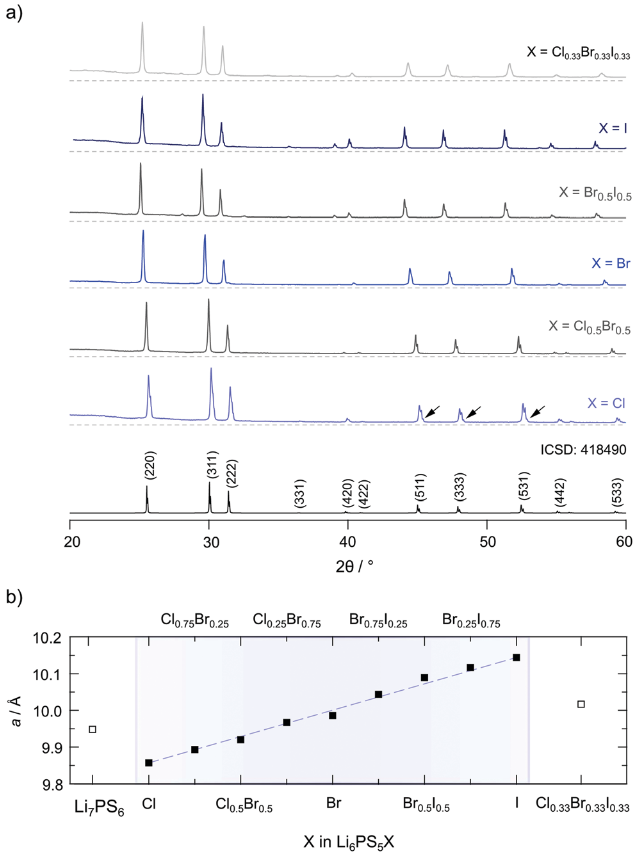

Fig. 2 (a) X-ray powder diffraction patterns of the Li_6PS_5X series investigated within this study (X = Cl, $Cl_{0.5}Br_{0.5}$, Br, $Br_{0.5}I_{0.5}$, I and $Cl_{0.33}Br_{0.33}I_{0.33}$). The XRPD patterns were recorded after the final annealing step at room temperature. In some cases, little, almost negligible, amounts of Li_3PO_4 and LiX are visible; the amount of LiX does not exceed 1.5 wt%. Only for Li_6PS_5Cl *ca.* 3.3 wt% Li_3PO_4 is seen, see the arrows; in all other cases its amount is negligible or less than 1.5 wt%, see the ESI† for Rietveld refinements (Fig. S1 and S2). (b) Lattice parameter of Li_6PS_5X obtained from Rietveld refinements of the patterns shown in (a). The lattice parameter increases continuously with the radius of X.

2 Experimental

2.1 Sample preparation through a solid state reaction

The Li argyrodites Li_6PS_5X, with the compositions shown in Fig. 2b, have been prepared by mixing stoichiometric amounts of Li_2S (Sigma-Aldrich $\geq$99.98%), P_2S_5 (Honeywell Fluka $\leq$99%) and LiCl (Sigma-Aldrich, anhydrous, 99%), LiBr (Sigma-Aldrich, anhydrous, 99.98%) and LiI (Sigma-Aldrich, 99.9%). The starting compounds were mechanically milled using a high-energy planetary ball mill (Fritsch Pulverisette 7 Premium line) at a rotation speed of 400 rpm for 4 hours (15 min milling; 15 min pause). Milling was carried out using ZrO_2 beakers (45 ml) filled with 180 balls (ZrO_2, 5 mm in diameter). Afterwards the mixtures were uniaxially pressed (0.4 tons) into pellets with a diameter of 5 mm, filled into quartz ampoules and sealed under a vacuum. The ampules were preheated at 573 K under a dynamic vacuum to remove traces of water. The reaction was carried out at 823 K (heating rate: 5 K min^{-1}, duration 7 days; cooling rate 10 K min^{-1}). All preparation steps were strictly carried out in an Ar gas atmosphere (H_2O < 1 ppm, O_2 < 1 ppm).

2.2 X-ray powder diffraction (XRPD)

The samples were analyzed by X-ray diffraction using a Bruker D8 Advance diffractometer (Bragg Brentano geometry, Cu K_α radiation). The patterns, shown in Fig. 2, were recorded with a step size of 0.02° (measuring time 2 s) in the 2θ-range 20° to 100°. Rietveld refinement, see Fig. 3 and the ESI† (Fig. S1 and S2), was carried out by using X'PertHighScorePlus (Panalytical).

2.3 Impedance spectroscopy

To measure the impedance responses of the pellets, Au electrodes were applied. We used a LEICA EM SCD 050 sputter coater to equip the samples with a thin Au layer of 100 nm thickness. Impedance spectra were recorded with a Novocontrol Concept 80 broadband dielectric spectrometer; the frequency range covered ranged from ν = 10 mHz to 10 MHz. The temperature T was varied from 173 K to 453 K in steps of 20 K; the temperature in the sample holder was controlled by a QUATRO cryosystem (Novocontrol) that uses freshly evaporated nitrogen and a heater to adjust the temperature with an accuracy of ±0.5 K. The measurements were carried out in a dry nitrogen atmosphere to avoid any contamination with water and oxygen.

2.4 ^{7}Li static NMR measurements

For the time-domain NMR measurements the samples Li_6PS_5Cl, Li_6PS_5Br and Li_6PS_5I were sealed in Duran© glass tubes (*ca.* 4 cm in length and 3 mm in diameter). They were kept under a vacuum to protect them from any reaction with humidity or traces of oxygen. We used ^{7}Li NMR line shape measurements and spin–lattice relaxation (SLR) experiments to collect information about Li activation energies and jump rates. Longitudinal NMR SLR rates ($1/T_1$) as well as spin-lock rates ($1/T_{1\rho}$)

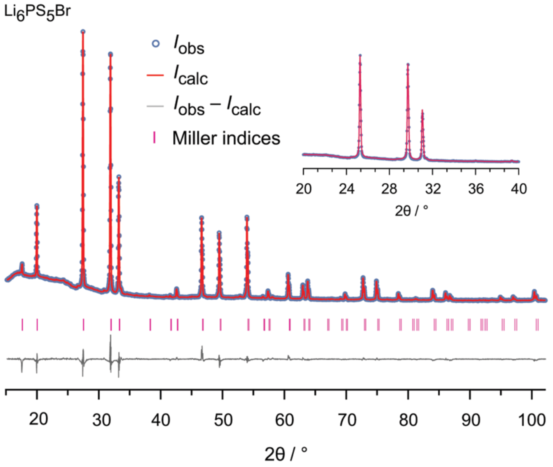

Fig. 3 Rietveld analysis of the XRPD pattern of Li_6PS_5Br recorded at 293 K (R_{Bragg} = 4.633%). In this plot the Bragg positions as well as calculated and observed profiles are depicted. The analysis reveals a phase pure sample. The R_w profile is 10.84% and the GoF amounts to 4.82; see the ESI† for further explanations.

were measured by employing a Bruker Avance III spectrometer connected to a shimmed cryomagnet with a nominal magnetic field of 7 T. This field corresponds to a ^{7}Li Larmor frequency of $\omega_0/2\pi$ = 116 MHz. For the measurements at temperatures T ranging from 173 K to 433 K a ceramic high-temperature probe (Bruker Biospin) was used. At a power level of 200 W the $\pi/2$ pulse length ranged from 2.7 to 3.2 μs slightly depending on temperature. A Eurotherm temperature controller in combination with a type T thermocouple was used to control and to monitor the temperature in the sample chamber. Low temperature measurements down to T = 124 K were performed with a cryo probe (Bruker) that uses freshly evaporated nitrogen to reach temperatures below ambient. The $\pi/2$ pulse length of the cryo probe ranged from 3.0 to 4.3 μs at a power level of 95 W. It is equipped with a LakeShore 331 element equipped with two Cernox temperature sensors.

^{7}Li NMR SLR rates $1/T_1 \equiv R_1$ in the laboratory frame were acquired with the well-known saturation recovery pulse sequence.[45,46] This sequence uses a comb of closely spaced $\pi/2$ pulses to destroy any longitudinal magnetization M_z. The subsequent recovery of M_z was detected as a function of waiting time t_d with a $\pi/2$ reading pulse: $10 \times \pi/2 - t_d - \pi/2 -$ acquisition.[15] To construct the magnetization transients $M_z(t_d)$, we plotted the area under the free induction decays (FIDs) *vs.* t_d. Up to 16 FIDs were accumulated for each waiting time.

The transients $M_z(t_d)$ were parameterised with stretched exponentials, $M_z(t_d) \propto 1 - \exp(-(t_d/T_1)^\gamma)$, to extract the SLR rates R_1. Additionally, rotating-frame ^{7}Li NMR SLRρ rates $1/T_{1\rho} \equiv R_1$ were measured by means of the spin-lock technique: $\pi/2 - p_{lock}$ acquisition. We used a locking frequency $\omega_1/2\pi$ of 20 kHz.[47,48] The duration t_{lock} of the locking pulse p_{lock} was varied between 22 μs and 460 ms. To ensure full longitudinal relaxation between each spin-lock scan the recycle delay was set to at least $5 \times T_1$. Again, the $R_{1\rho}$ rates were obtained by analysing the resulting transients $M_\rho(t_{lock})$ with stretched exponentials of the form $M_\rho(t_{lock}) \propto \exp(-(t_{lock}/T_{1\rho})^\kappa)$. While the stretching exponents γ varied from 1 to 0.9, the exponents κ range from 0.4 to 1, depending on the temperature. Some of the $T_{1\rho}$ transients showed bi-exponential behaviour and were analyzed with a sum of two stretched exponential functions.

2.5 Magic angle spinning (MAS) NMR

^{6}Li (73.6 MHz), ^{31}P (202.4 MHz), ^{127}I (100.1 MHz), ^{79}Br (125.3 MHz) and ^{35}Cl (49.0 MHz) NMR spectra under magic angle spinning (MAS) conditions were recorded with a 500 MHz Avance spectrometer (Bruker). The high-resolution MAS NMR spectra were measured at a rotation speed of 25 kHz using 2.5 mm rotors with an ambient bearing gas temperature. Spectra were recorded with a single pulse sequence. We accumulated up to 128 scans for one spectrum. LiCl, KBr, LiI and 85% H_3PO_4 served as ref. 31 to determine chemical shifts δ_{iso}. In order to detect also very slow diffusion processes and to obtain quantitative MAS NMR spectra we varied the recycle delay from 1 s to 180 s. Sufficiently long relaxation delays guarantee full longitudinal relaxation of all spectral components. Further information on pulse lengths, temperature effects and delay times are given in the ESI,† see Table S1.

3 Results and characterization

3.1 Sample characterization by X-ray powder diffraction

To study the ion dynamics in argyrodite-type Li_6PS_5X we used a solid-state synthesis approach to prepare samples with the following compositions: X = Cl, $Cl_{0.75}Br_{0.25}$, $Cl_{0.5}Br_{0.5}$, $Cl_{0.25}Br_{0.75}$, Br, $Br_{0.75}I_{0.25}$, $Br_{0.5}I_{0.5}$, $Br_{0.25}I_{0.75}$, I and X = $Cl_{0.33}Br_{0.33}I_{0.33}$, respectively. Through replacing S^{2-} with X^- we change the average lattice constant of the crystal structure, the polarisability of the anion lattice and the degree of anion disorder. The relative density of our samples, estimated from the sintered pellets used for impedance spectroscopy, reached values ranging from 92% to 98%. Argyrodite-type Li_6PS_5X is expected to crystallise with cubic $F\bar{4}3m$ face centered (fc) symmetry; the crystal structure is depicted in Fig. 1.

In Fig. 2a the XRPD patterns of all samples are shown including a reference pattern taken from the literature (entry no. 418490 in the inorganic crystal structure database (ICSD)). The positions and intensities of the reflections obtained for the different patterns of Li_6PS_5X including Li_7PS_6 match very well with what is expected from the literature. Humps at low diffraction angles originate from the mercapto foil used to protect the samples from reaction with air during the measurements.

To characterise the samples in detail, Rietveld refinements were carried out. As an example, the result of the analysis is shown for Li_6PS_5Br in Fig. 3. The Li_6PS_5Br sample is phase pure and crystallises with cubic symmetry (space group $F\bar{4}3m$); the lattice parameter turned out to be a = 9.986 Å. The same symmetry is found for the other samples; the amount of side phases or impurities turned out to be extremely low, see the ESI.† When going from Li_6PS_5Cl to Li_6PS_5I the lattice parameter a increases from a = 9.857 Å to a = 10.145 Å. Lattice expansion of the unit cell is expected because the radius r of the anion increases in the order $r_{\mathrm{Cl}} < r_{\mathrm{Br}} < r_{\mathrm{I}}$. Here, an increasing unit cell volume stabilises the lithium ions in the transition state 24g; the change in lattice constant a seems to also affect the Li occupancies in the Li_6PS_5X series as has been shown by neutron diffraction.[34]

Recent neutron and X-ray synchrotron diffraction studies have shown that in fc cubic argyrodite-type Li_6PS_5Cl and Li_6PS_5Br the S^{2-} and X anions can occupy three different crystallographic positions. Whereas the 16e site is fully occupied by S^{2-} anions, the sites 4a and 4d are shared by the S^{2-} and X anions. For Li_6PS_5Cl Kraft *et al.* found that 38.5% of the 4a site and 61.5% of the 4d site is occupied by Cl^-.[34] The rest is filled by S^{2-} anions; Li^+ only occupies the 48h sites. For Li_6PS_5Br Rietveld analysis yielded occupancies of 77.9% (4a) and 22.1% (4d) with Li^+ distributed over the 48h (44.1%) and 24g (11.9%) sites. Thus, the highest degree of anion disorder is found for Li_6PS_5Cl, while cation disorder for the samples rich in Br. This finding is in contrast to what Rietveld refinement resulted in for Li_6PS_5I. While Li disorder is also present for the split-site (48h (39.1%) and 24g (21.9%)), in Li_6PS_5I the I anions solely occupy the 4a sites. The 4d sites are fully occupied by S^{2-}. Deiseroth and co-workers also reported on the same order/disorder effects earlier.[31,40,49]

The larger difference in ionic radii between I^- and S^{2-} ($r_{\mathrm{I^-}}$ = 216 pm *vs.* $r_{\mathrm{S^{2-}}}$ = 184 pm, as compared to $r_{\mathrm{Cl^-}}$ = 181 pm and $r_{\mathrm{Br^-}}$ = 195 pm) might lead to this site preference for the anions. The anion sublattice in Li_6PS_5I is, thus, structurally ordered as compared to Li_6PS_5Cl (and Li_6PS_5Br); simultaneously, cation disorder shows up for Li_6PS_5Br and Li_6PS_5I.[36,37,50] The compounds with mixed halogen compositions agree well with the trend in S^{2-}/X occupancy and cation disorder.[34] As will be discussed below, anion ordering seems to have an important impact on long-range ion diffusion in the I compound.

The 24g site represents an intermediate state used by the Li ions on 48h to diffuse through. As a result of these two lithium positions three different jump processes can occur; they are explicitly shown in Fig. 1b. (i) A strongly localised process is given by 48h–24h–48h′ jumps. Intracage jumps are possible within the octahedral cage when the Li ions jump between the 48h sites: (ii) 48h–48h″. (iii) Long-range ion dynamics needs $48h_1$–$48h_2$ intercage jump processes between two different cages 1 and 2. The latter jump process is expected to be strongly affected by the anion site disorder of X and S^{2-}. We expect that a high degree of substitutional disorder will have a significant impact on the associated jump rate, which characterises exchange processes between the cages.

3.2 Magic angle spinning NMR

To investigate local structures of the argyrodites, we recorded ^{31}P (spin-quantum number $I = 1/2$) MAS NMR spectra of Li_6PS_5X (X = Cl, Br, I) at a spinning speed of 25 kHz. The spectra are shown in Fig. 4a. In line with the report of Deiseroth and co-workers,[31] the ^{31}P MAS NMR resonance of Li_6PS_5I shows a very sharp line centered at δ_{iso} = 96.3 ppm pointing to an ordered anion framework with the I anions non-randomly occupying selected crystal sites. Small shoulders near the main signal might point to defect sites in Li_6PS_5I.

The ^{31}P MAS NMR spectrum of Li_6PS_5I is in stark contrast to the situation that is met for Li_6PS_5Cl, for which we expect the influence of strong S/Cl disorder on the line shape, see above. Indeed, its very broad line, which can hardly be resolved,

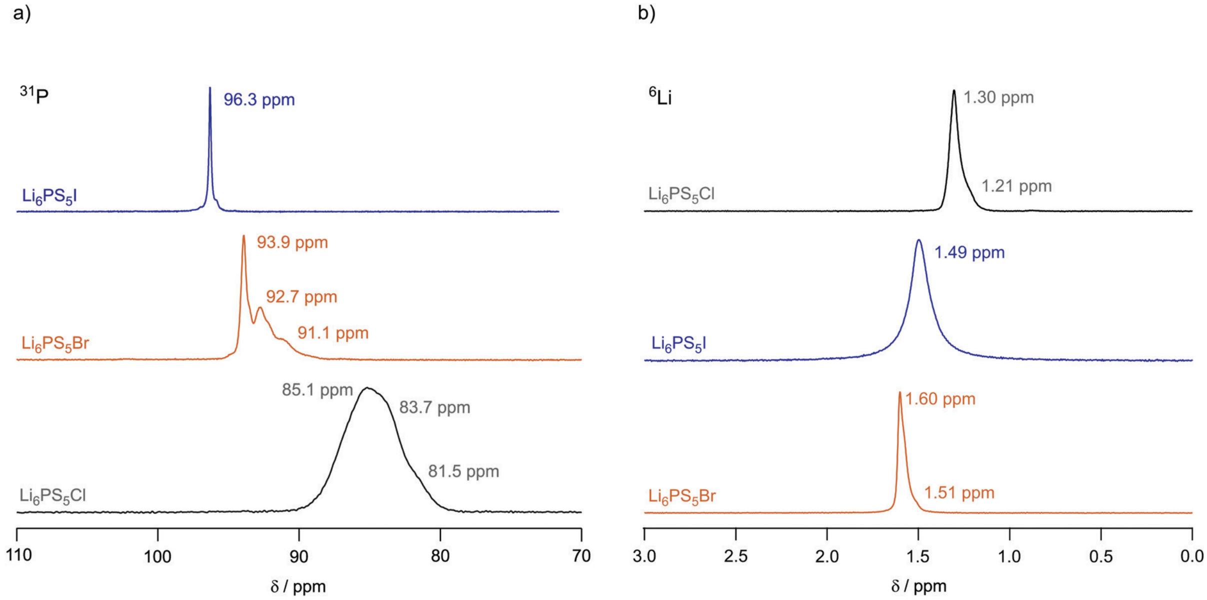

Fig. 4 (a) ^{31}P MAS NMR spectra of Li_6PS_5I, Li_6PS_5Br and Li_6PS_5Cl recorded at 202.4 MHz and a spinning frequency of 25 kHz. The spectra have been referenced to 85% H_3PO_4 and were recorded at an ambient bearing gas temperature.[31] (b) ^6Li MAS NMR spectra of Li_6PS_5Cl, Li_6PS_5Br and Li_6PS_5I recorded at 73.6 MHz and a spinning speed of 25 kHz. All spectra have been referenced to solid $LiCH_3COO$. Values given in ppm indicate the isotropic chemical shifts.

reveals a wide distribution of chemical shifts and strong spin–spin interactions. Chemical shifts of lines constituting the overall line range from 85 to 81 ppm. Therefore, ^{31}P MAS NMR clearly reveals anion disorder in Li_6PS_5Cl. The ^{31}P MAS NMR line of Li_6PS_5Br takes an intermediate position. It is composed of narrower lines than those seen for Li_6PS_5Cl; nevertheless, line broadening, as compared to Li_6PS_5I, reveals disorder in the S/Br sublattice. At least the spectrum is composed of three distinct lines located at 93.9 ppm, 92.7 ppm and 91.1 ppm, respectively. The same increase in substitutional disorder might be seen if we consider the corresponding ^{127}I, ^{79}Br and ^{35}Cl MAS NMR spectra of the three compounds; the corresponding spectra of the three quadrupole nuclei are shown in the ESI,† Fig. S3. Clearly, because of the large quadrupole moment of I ($|Q(^{127}I)| = 0.721b$) the full spectrum including its spinning side bands is rather broad. The isotropic signal, however, is much smaller than that for Li_6PS_5Cl and Li_6PS_5Br with $|Q(^{35}Cl)| = 0.855b$ and $|Q(^{79}Cl)| = 0.330b$. Although exposed to less second order quadrupole effects, the line of Li_6PS_5Cl is as broad as that of the Br compound. Site disorder in Li_6PS_5Cl might explain this additional broadening.

The ordered anion framework seen for Li_6PS_5I by ^{31}P MAS NMR, synchrotron X-ray diffraction and neutron diffraction[34] is fully consistent with results from ^{7}Li SLR NMR on the ion dynamics in the I compound. As we will show and discuss below, an almost symmetric diffusion-induced ^{7}Li NMR rate peak describes longitudinal spin–lattice relaxation in Li_6PS_5I; Li^+ disorder on the split-site does not influence this symmetry. This observation mainly points to the absence of pronounced site disorder in the anion sublattice. Structural anion disorder is, thus, expected to have a significant impact on both the Li ion diffusion and ionic conductivity in Li_6PS_5X.

For the sake of completeness, we also recorded ^{6}Li ($I = 1$) MAS NMR spectra at an ambient bearing gas temperature, these spectra are shown in Fig. 4b. They have been referenced to $LiCH_3COO$. For Li_6PS_5Br and Li_6PS_5Cl we observe a slightly asymmetric line with chemical shifts of $\delta_{iso} = 1.6$ ppm and $\delta_{iso} = 1.3$ ppm, respectively. The line of Li_6PS_5I turned out to be more symmetric in shape and is broader than the other lines. As Li_6PS_5Br and Li_6PS_5Cl show rapid Li ion long-range translational dynamics their lines represent already coalesced spectra at the measurement temperature of 307 K, see the ESI.† This observation is in perfect agreement with ^{7}Li NMR motional line narrowing (see below), which has reached its extreme limit already well below ambient temperature.

In contrast, complete line narrowing of the static ^{7}Li NMR line of Li_6PS_5I is shifted toward much higher temperature, revealing significantly slower long-range ion dynamics (*vide infra*). In addition, the absence of effective Li ion dynamics in Li_6PS_5I, which would be able to also average (small) second order quadrupolar interactions that the spin-1 nucleus ^{6}Li is exposed to, might further increase the width of the NMR line of Li_6PS_5I as compared to the samples with X = Cl or Br. The increased anisotropy seen for Li_6PS_5Cl is in line with the degree of site disorder in Li_6PS_5Cl and Li_6PS_5Br.

Interestingly, according to the halogen anion introduced into the argyrodite struture the isotropic chemical shift values δ_{iso} of the ^{6}Li MAS NMR spectra increase from Li_6PS_5Br to Li_6PS_5I and further to Li_6PS_5Cl. Thus, the paramagnetic component of the NMR line decreases; obviously, the different halogen anions change the electron density distribution in the direct neighborhood of the Li spins with Li_6PS_5Br having the highest density.

3.3 Ion dynamics as seen by conductivity spectroscopy

We used broadband impedance spectroscopy[51–53] covering frequencies from the mHz to the MHz region to study the ion dynamics in Li_6PS_5X to see the change in the overall ionic transport properties with the X substitution. As an example, in Fig. 5a the real part σ' of the complex conductivity $\hat{\sigma}$ of Li_6PS_5Br is plotted *vs.* the frequency ν.

At low frequencies and high temperatures T the isotherms $\sigma'(\nu)$ reveal electrode polarization, which results from the accumulation of ions at the surface of the ion blocking electrodes applied.[52–54] Towards higher frequencies or at sufficiently low T, distinct direct current (DC) plateaus show up, which reflect long-range ion transport. The corresponding σ_{DC} value is governed by both bulk and grain boundary contributions. For the bromide sample, Li_6PS_5Br, $\log_{10}(\sigma_{DC})T$ follows Arrhenius behaviour

$$\sigma_{DC}T = \sigma_0 \exp(-E_{a,DC}/(k_BT)) \tag{1}$$

with an activation energy, $E_{a,DC}$, as low as 0.296 eV. The corresponding Arrhenius line is shown in Fig. 5b. Almost the same behaviour is seen for $Li_6PS_5Cl_{0.5}Br_{0.5}$. Going back to the underlying isotherms $\sigma'(\nu)$ we clearly observe dispersive regions at very low T and high frequencies ν. These regions can be approximated by a Jonscher-type power law, $\sigma' = \sigma_{DC} + A\nu^p$, where A is the alternating current coefficient and p represents the power law exponent. Because of the very high ionic conductivity of Li_6PS_5Br, this behaviour, influenced by short-range ion dynamics including forward–backward jump processes, is only seen at temperatures below 193 K.[52,54] Here, p turned out to be *ca.* 0.75; such a value is expected for 3D correlated motion.[55] Similar isotherms were observed for the other compositions investigated.

For comparison, in Fig. 5b the temperature dependence of $\log_{10}(\sigma_{DC})T$ of the other samples is presented. Li_6PS_5I and Li_7PS_6 are characterised by the lowest conductivities and the highest activation energies $E_{a,DC}$ of 0.47 eV and 0.37 eV. At approximately 250 K we notice a slight deviation from the Arrhenius line determining $\log_{10}(\sigma_{DC})T$ at higher T. This behaviour cannot be related to the phase transition of Li_6PS_5I;[31,39,40,49] the I compound transforms into a low-T phase at $T \approx 160$ K, see below. Such a slight deviation is also seen for Li_6PS_5Cl.

In Fig. 6a the changes in activation energies, ionic conductivities and Arrhenius pre-factors (σ_0, see eqn (1)) are illustrated. In all cases, the replacement of sulfur anions in Li_7PS_6 by heavier halide anions leads to a decrease in activation energies. Except for Li_6PS_5Cl and $Li_6PS_5Cl_{0.75}Br_{0.25}$ the Arrhenius pre-factor σ_0 also decreases. This feature, which is seen when Li_6PS_5Br is compared with Li_7PS_6 (or Li_6PS_5Cl), has been interpreted in terms of the Meyer–Neldel[56] rule and related to a reduction in

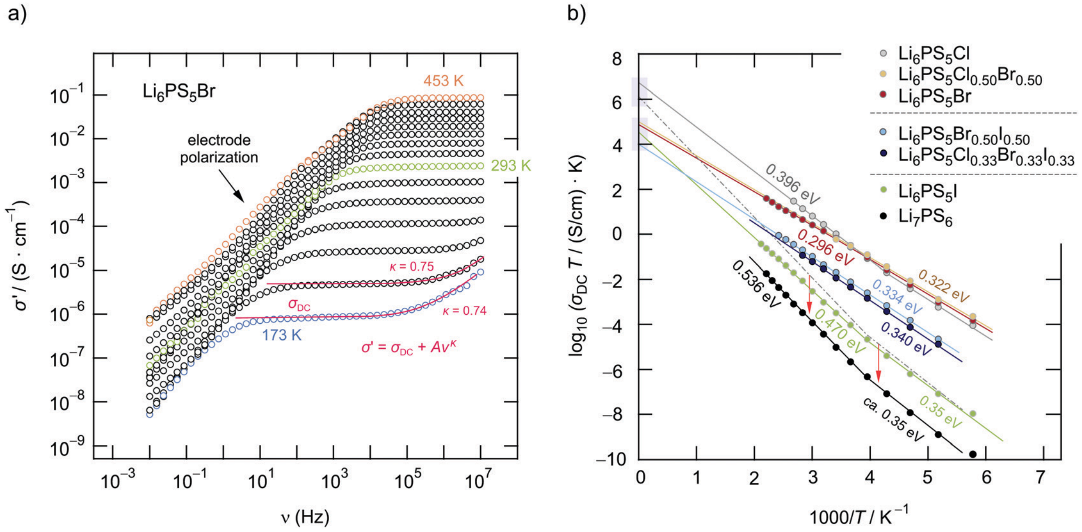

Fig. 5 (a) Conductivity isotherms (10 mHz to 10 MHz) of Li_6PS_5Br at temperatures ranging from 173 K to 453 K; isotherms have been recorded in steps of 20 K. (b) Change of the DC conductivity of Li_6PS_5X as a function of inverse temperature. The highest conductivity is found for Li_6PS_5Cl and the lowest for Li_6PS_5I. Data points and the Arrhenius line referring to Li_7PS_6 have an offset of −2 on the log scale for the sake of clarity.

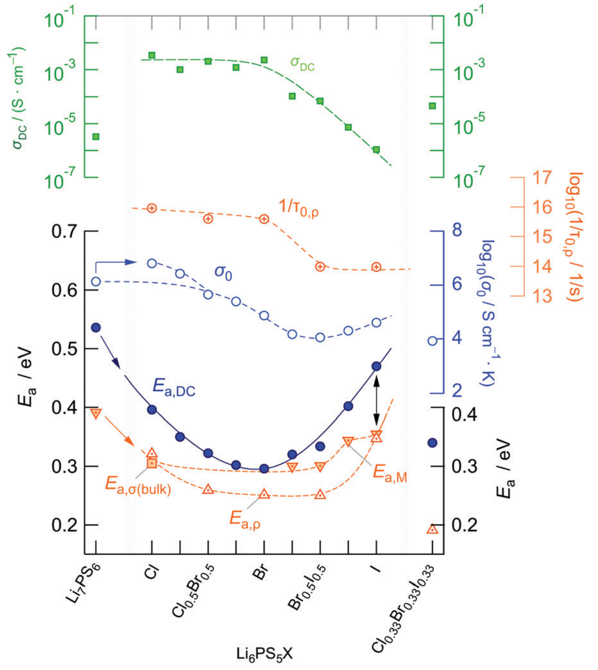

Fig. 6 Activation energies $E_{a,DC}$ of the argyrodite samples prepared. $E_{a,DC}$, determined with the help of conductivity isotherms, characterises the overall ion transport, which is affected by both bulk and g.b. contributions. A minimum is found for Li_6PS_5Br. The dependence of the corresponding Arrhenius pre-factor on anion substitution is also shown. For the sake of completeness, we also included activation energies that, most likely, describe bulk ion dynamics. These have been extracted either (i) from conductivity isotherms (Li_6PS_5Cl), (ii) from modulus spectra or (iii) from variable-temperature resistivity measurements carried out at fixed frequencies (see below). In the upper graph overall ionic conductivities at room temperature are shown. The highest conductivity of 3×10^{-3} S cm^{-1} has been observed for Li_6PS_5Cl, whereas Li_6PS_5I reveals the lowest overall conductivity of only 10^{-6}.

Debye frequencies for soft lattices created by substitution of Br and I for S.[34] If we compare our results for Li_6PS_5Cl with respect to the conductivity behaviour of Li_7PS_6 we witness both a decrease in $E_{a,DC}$ from 0.536 eV to 0.396 eV and an increase in σ_0 by one order of magnitude. This favorable combination of $E_{a,DC}$ and σ_0 results in a room temperature ionic conductivity of σ_{DC} = 3.8 mS cm^{-1}. For Li_6PS_5Br, with its more polarisable anions on the other hand, the low activation energy is compensated by a pre-factor two orders of magnitude lower than that for Li_6PS_5Cl. Considering high temperatures this feature causes σ_{DC} to adopt values lower than those of Li_6PS_5Cl.

Interestingly, the ionic conductivity of ordered Li_6PS_5I is even lower than that of the non-substituted compound Li_7PS_6; this decrease, despite the higher activation energy found for Li_7PS_6, can also be explained by the relatively low value for σ_0. The pre-factor is proportional to the attempt frequencies ν_a, the number of effective charge carriers n_{Li} and an entropy term.[42] Besides the effect of ν_a, trapping effects in Li_6PS_5I, because of a very low intercage jump rate, might reduce N for this sample. If we assume similar ν_a values for Li_6PS_5Cl and Li_6PS_5Br, entropy effects could serve as an explanation for the change in σ_0. Especially for the highly disordered Li_6PS_5Cl sample[50] the migration entropy might take a decisive role in influencing the ion dynamics. For the ordered Li_6PS_5I compound this contribution might be absent.

When going from Li_6PS_5Br to Li_6PS_5I we see that, despite the introduction of polarisable iodine anions, the pre-factor remains almost the same, $A = \log(\sigma_0/(\text{S cm}^{-1}\ \text{K})) = 4.9$ for Li_6PS_5Br and $A = 4.6$ for Li_6PS_5I, but $E_{a,DC}$ increases from 0.296 eV to 0.47 eV. From this point of view, although the lattice gets softer in the case of I, Kraft *et al.* mentioned[34] that Meyer Neldel seems to be not fully applicable to describe the situation in Li_6PS_5I. One could have expected the more polarisable I anions to allow the Li ions to squeeze through smaller voids.[50] Obviously, this concept does not work for Li_6PS_5Br and Li_6PS_5I, at least if we regard the (overall) averaged long-range ion transport process as probed by σ_{DC} measurements.

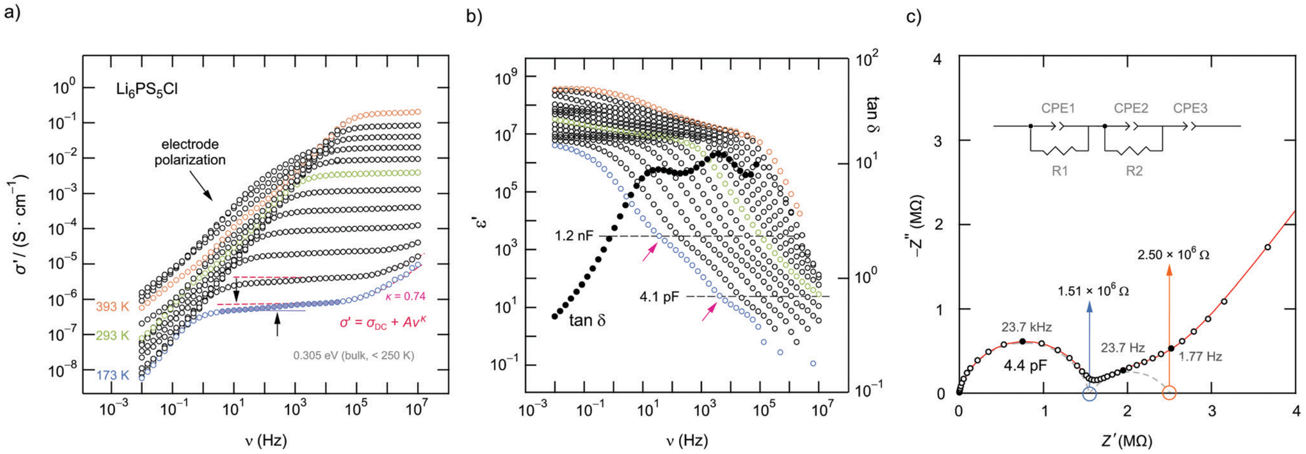

Fig. 7 (a) Conductivity isotherms of Li_6PS_5Cl recorded at temperatures ranging from 173 K up to 393 K. Jonscher-type power laws are used to parameterise the dispersive regions seen at the lowest temperatures. At sufficiently low T we notice a step in the DC plateaus that is attributed to contributions from grain boundaries and the bulk regions. (b) Real part of the permittivity (and loss factor (173 K)) plotted as a function of frequency. Disregarding the polarisation regime, ε' also reveals a two-step frequency decay characterised by the following capacitances: 4.1×10^{-12} F and 1.2×10^{-9} F. Dots show the change of the loss factor $\tan\delta$ passing through two maxima. (c) Complex plane plot (Nyquist plot) of the real part Z' *vs.* the imaginary part Z'' of the complex impedance $\hat{Z}$ of a Li_6PS_5Cl pellet (173 K). Two depressed semicircles are seen reflecting the bulk (4.4×10^{-12} F) and grain boundary response (6.8×10^{-9} F).

The ionic conductivities of the mixed compounds containing I anions, *viz.* $Li_6PS_5Br_{0.5}I_{0.5}$ and $Li_6PS_5Cl_{1/3}Br_{1/3}I_{1/3}$, do not vary much. Obviously, the introduction of I plays the crucial role to lower σ_{DC}. The Cl anions do not affect the ionic transport in these high-entropy compounds in a positive way, at least for compounds containing two anions greatly differing in ionic radius (181 pm *vs.* 216 pm). To take a closer look at the exceptional behaviour of Li_6PS_5Cl with its high degree of anion disorder we tried to separate the bulk and grain boundary contributions of this sample. Moreover, we used complex resistivity measurements to further characterise the ion dynamics.

The $\sigma'(\nu)$ isotherms of Li_6PS_5Cl are shown in Fig. 7a. A careful look at the DC plateau region shows that it contains a small step. Thus, it is composed of actually two plateaus. Below 250 K, the corresponding activation energies turned out to be 0.310 eV and 0.305 eV, see Fig. 7b. The two-step behaviour of the $\sigma'(\nu)$ isotherms of Li_6PS_5Cl are also seen if we plot the real part ε' of the complex permittivity *vs.* ν (Fig. 7b). We used the equation for a parallel-plate capacitor to estimate the corresponding capacitance C of the two steps:

$$C = \varepsilon_0\varepsilon_r \cdot \frac{A}{d} \qquad (2)$$

Here ε_0 represents the electric field constant (8.854×10^{-12} F m^{-1}), and A is the area and d the thickness of the sample. While the first DC plateau at high frequencies is characterised by C_1 = 4.1 pF, for the one at lower ν we found C_2 = 1.2 nF. Therefore, the plateau associated with C_1 in the pF range represents the bulk response, whereas the response at lower frequencies is governed by grain boundary contributions for which capacitances typically in the nF regime are expected.[57] The estimated capacitances are in good agreement with those that can be inferred from complex plane plots (Fig. 7c). At 173 K the corresponding Nyquist plot is dominated by two depressed semicircles; electrode polarization shows up at low frequencies. If we calculate C *via* $\omega_{el} = 1/RC$, where $\omega_{el} = 2\pi\nu_{el}$ is the electric relaxation frequency and R the resistance at the intercept of the curve with the Z' axis,[57] we obtain C_1 = 4.4 pF and C_2 = 6.8 nF, being in good agreement with the estimation presented above. Only for Li_6PS_5Cl we managed to separate the small difference between the bulk and g.b. contributions. Also for Li_6PS_5I this difference is expected to be very small.

For comparison, the two contributions in the electrical relaxation of Li_6PS_5Cl are also seen in the loss factor $\tan\delta = \varepsilon''/\varepsilon'$ when plotted as a function of frequency ν (see also Fig. 7b). The maxima in $\tan\delta$, showing up at 15.36 Hz (g.b.) and 4.21 kHz (bulk), correspond to the plateaus or inflection points of $\varepsilon'\nu$, see also Fig. 8. According to $\hat{\sigma} = i\omega\varepsilon_0\hat{\varepsilon} = i\omega\varepsilon_0\varepsilon' + \omega\varepsilon_0\varepsilon''$ the maxima in $\tan\delta$ produce two minima if the frequency dependence of the imaginary part $\sigma''(\propto\varepsilon')$ is analyzed (Fig. 8).

To further characterise ion hopping in Li_6PS_5X, especially if we consider samples with lower conductivity than Li_6PS_5Cl and

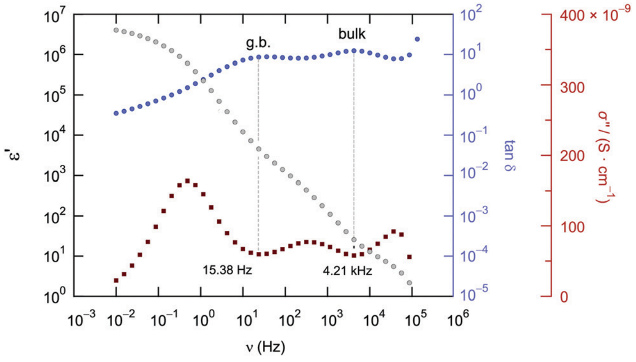

Fig. 8 Comparison of the frequency dependence of $\tan\delta$, ε' and σ'' of Li_6PS_5Cl measured at 173 K. Plateaus (or inflection points) in ε' result in minima in σ'' and maxima in $\tan\delta$, respectively.

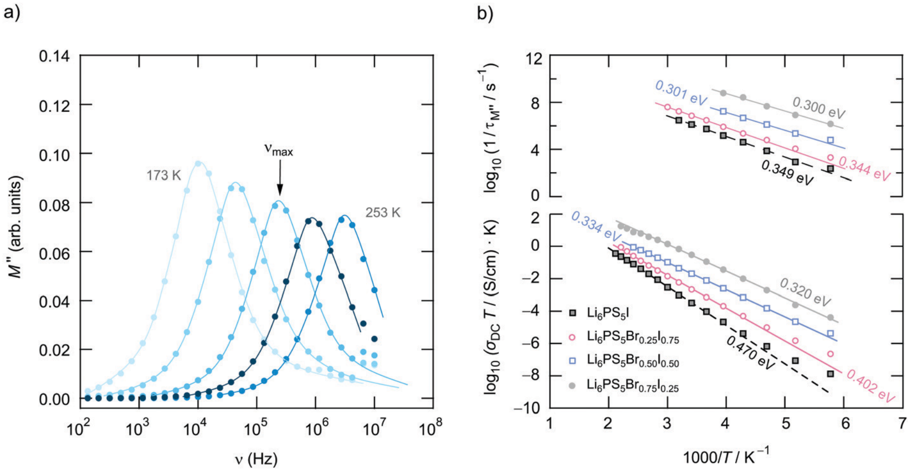

Fig. 9 (a) Frequency dependence of the imaginary part of the modulus, M'', of $Li_6PS_5Br_{0.50}I_{0.50}$ recorded from 173 K to 253 K in steps of 20 K. The lines are to guide the eye. The temperature dependence of the rate $\tau_M{}^{-1}$ is shown in (b). For comparison, the results for $Li_6PS_5Br_{0.25}I_{0.75}$, $Li_6PS_5Br_{0.75}I_{0.25}$ and Li_6PS_5I are also included. The lower part of the graph shows $\sigma_{DC}T(1/T)$; the values given represent activation energies. For the sake of clarity, data of $Li_6PS_5Br_{0.75}I_{0.25}$ (solid line, grey) have been plotted using an offset of +1 on the log scale.

Li_6PS_5Br, we used the electric modulus representation[58,59] to take a look at electrical relaxation frequencies $\tau_{M''}{}^{-1} = \nu_{max}$. As an example, in Fig. 9 for $Li_6PS_5Br_{0.5}I_{0.5}$ the imaginary part M'' of the complex modulus is plotted *vs.* ν. Since the amplitude of M'' is proportional to $1/C$, bulk processes are mainly seen. For samples with very high conductivities, such as Li_6PS_5Cl, the peaks are shifted to too high frequencies and are, thus, no longer fully visible. Activation energies $E_{a,M''}$ from our $M''(\nu)$ analysis are also included in Fig. 6. For comparison, the bulk activation energy deduced from Fig. 7 is included, too. They reveal that the activation energies, which we ascribe to bulk properties, do not change much if we consider compounds up to the composition $Li_6PS_5Br_{0.5}I_{0.5}$. This behaviour changes if we increase the I concentration. Importantly, for the compounds rich in I, especially if we consider Li_6PS_5I, the observation $E_{a,M''} < E_{a,DC}$ suggests that the charge carrier concentration increases with temperature. For Li_6PS_5I the difference $E_{a,DC} - E_{a,M''}$ turned out to be relatively high, *viz.* 0.121 eV (see the vertical arrow in Fig. 6).

Additionally, after we took a look at the overall and bulk ion dynamics in Li_6PS_5X we used complex resistivity measurements, $\hat{\rho} = 1/\hat{\sigma} = \hat{M}/(i\omega\varepsilon_0)$, carried out at constant frequency but varying temperature, to answer the question of how the bulk ion dynamics depends on the time-scale and length-scale that the technique applied is sensitive to. In Fig. 10a the temperature dependence of the real part $\rho' = M''/\omega$ of the complex resistivity $\hat{\rho}$ is shown for Li_6PS_5Br. The peaks in Fig. 10a have been recorded for two different frequencies *viz.* 1 MHz and 10 MHz.

ρ' is given by a Lorentzian-shaped function containing the electrical relaxation time τ_ρ:[60]

$$\rho' \propto \frac{\tau_\rho}{1 + (\omega\tau_\rho)^{\beta'}} \tag{3}$$

The quantity $\log_{10}(M''/\omega)$ when plotted *vs.* $1/T$ shows similar features to the diffusion-induced NMR spin–lattice relaxation rate.[15,51,60] The higher the frequency the more the peaks shift towards higher temperatures. Symmetric peaks are obtained for $\beta' = 2$; if $\beta' < 2$ the low-T flank becomes lower than that of the high-T side. Indeed, for Li_6PS_5Br we notice an asymmetric peak that strongly points to correlated motion in disordered ion conductors.[15,61–64] While the high-T flank yields an activation energy $E_{a,\rho}$ comparable to $E_{a,DC}$ when bulk processes are probed, short-range motions are seen on the low-T side. The latter motions are characterised by values as low as 0.15 eV, which are also seen for Li_6PS_5Cl and $Li_6PS_5Br_{0.5}I_{0.5}$ (Fig. 10b). $E_{a,\rho}$ of Li_6PS_5Cl is only slightly higher than $E_{\sigma,bulk}$ = 0.305 eV (see above).

We cannot see any strong variation in $E_{a,\rho}$ when comparing the response of $Li_6PS_5Br_{0.5}I_{0.5}$ with that of Li_6PS_5Br. $E_{a,\rho}$ values have also been included in Fig. 6; for the sake of clarity, they are separately shown in Fig. 10c. Obviously, a lower pre-factor of the underlying Arrhenius relation is responsible for this shift. The same effect is seen for Li_6PS_5I. Although the lattice is expected to be much softer in the case of Li_6PS_5I as compared to the situation in Li_6PS_5Cl, $\rho(\omega)$ tells us that the activation energies $E_{a,\rho}$ of the two compounds are very similar (0.32 eV *vs.* 0.35 eV). However, the peak $\rho'(\omega)$ of Li_6PS_5I is clearly shifted toward higher T and shows up at 385 K; the origin of this difference has to be looked for in the bulk ion dynamics, g.b. resistances cannot explain it. As compared to the peak of Li_6PS_5Cl the peak of the I compound is symmetric in shape ($\beta \approx 1.95$) and points to an ordered structure.

Obviously, as in the case of $E_{a,DC}$ the reason for the lower conductivity and, thus, the slower bulk electrical relaxation in Li_6PS_5I (and in $Li_6PS_5Br_{0.5}I_{0.5}$) has been looked for in the prefactor of the underlying Arrhenius relationships. Most likely, the anion site disorder in Li_6PS_5Cl is responsible for this behaviour. Indeed, if we approximate the $\rho'(\nu)$ peaks with eqn (3) we can extract pre-factor $\tau_{0,\rho}{}^{-1}$ assuming $\tau_\rho{}^{-1}$ to be depending on temperature according to Arrhenius. $\tau_{0,\rho}{}^{-1}$ values are also included in Fig. 6; indeed, they clearly reveal lower pre-factors for Li_6PS_5I by approximately two orders of magnitude. If we assume that the attempt frequencies are similar for Li_6PS_5Cl and

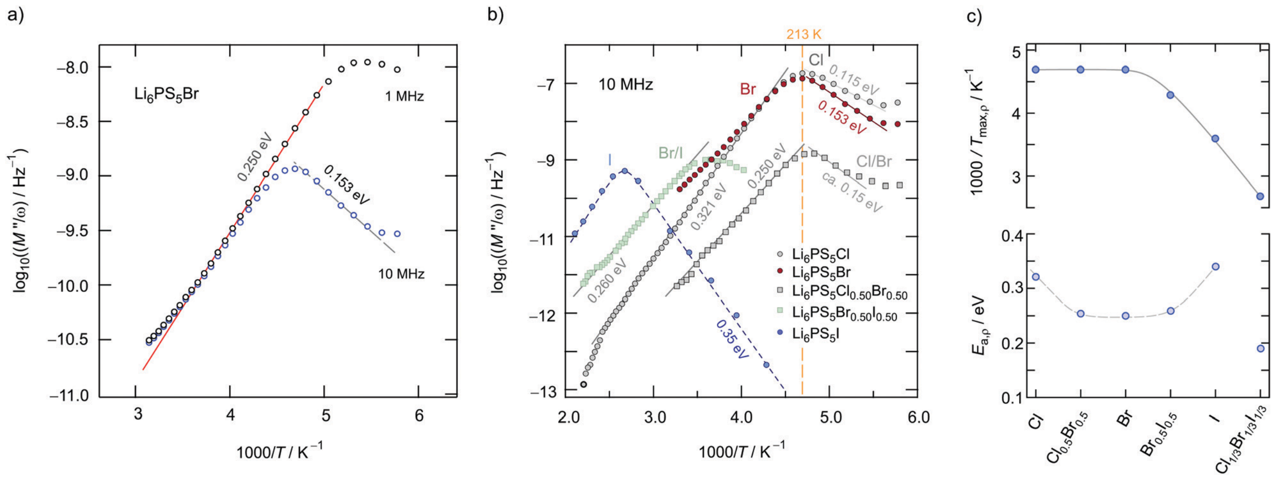

Fig. 10 (a) Real part of the complex resistivity ρ' of Li_6PS_5Br, measured at a fixed frequency (1 MHz and 10 MHz), *vs.* 1000/*T*. (b) $\rho'(\omega)$ peaks (10 MHz) of the argyrodites indicated. Asymmetric peaks point to time-scale dependent (heterogeneous) ion dynamics with local jump processes characterised by activation energies as low as 0.115 eV (Li_6PS_5Cl). (c) Temperatures (shown as 1000/*T*) at which the $\rho'(\omega)$ peaks show up. For Li_6PS_5I the peak is clearly shifted toward higher *T* indicating much slower ion dynamics. The change in $E_{a,\rho}$ is also shown.

Li_6PS_5I a significant change in migration entropy, as mentioned above, might explain the prominent change seen. To check whether this phenomenon is also apparent in SLR NMR, which is in general sensitive to both short-range and long-range ion dynamics, we carried out ^{7}Li NMR measurements in both the laboratory and rotating-frame of reference.[64,65] Line shape measurements carried out at temperatures down to the cryogenic region complement our investigation.

3.4 ^{7}Li NMR relaxometry to probe the bulk ion dynamics

In Fig. 11 an overview of the ^{7}Li NMR spin–lattice relaxation rates $1/T_1 \equiv R_1$ and $1/T_{1\rho} \equiv R_{1\rho}$ measured over a wide temperature range is given. To identify the thermally activated regions the rates of Li_6PS_5X, with X = Cl, Br, and I, were plotted using an Arrhenius representation, *i.e.*, $\log(1/T_1)$ is plotted *vs.* 1000/*T*. The rates have been recorded at a Larmor frequency of $\omega_0/2\pi$ = 116 MHz; for the locking frequency we used a magnetic B_1 field corresponding to $\omega_1/2\pi$ = 20 kHz. At very low temperatures (T < 160 K) the R_1 rates shown in Fig. 11a reveal a non-diffusive background; in this *T* range longitudinal relaxation is primarily induced by lattice vibrations or coupling of the Li spins (I = 3/2) with paramagnetic impurities.[61,65–67]

At higher *T* we expect spin–lattice relaxation to be increasingly induced by Li self-diffusion.[61] Indeed, the rates sharply increase

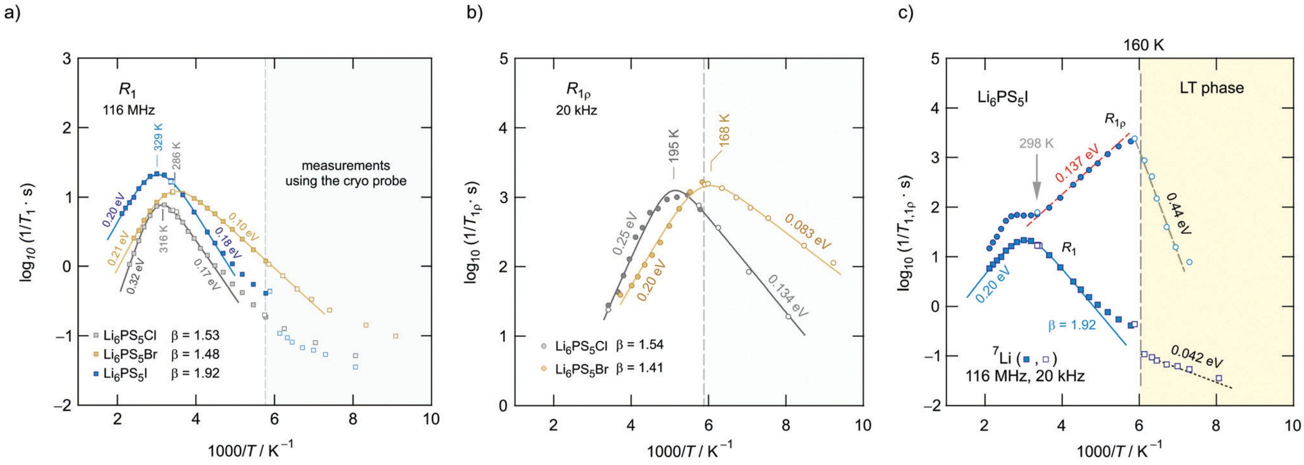

Fig. 11 (a) Temperature dependence of the diffusion-induced ^{7}Li NMR spin–lattice relaxation rates R_1 (116 MHz) of Li_6PS_5X (X: Cl, Br and I). Solid lines refer to BPP-type fits to extract activation energies and pre-factors. (b) Arrhenius plot of the corresponding ^{7}Li SLRρ NMR rates recorded in the rotating frame of reference using a nominal locking frequency of $\omega_1/2\pi$ = 20 kHz. Again, the solid lines represent fits according to a modified BPP relaxation model taking into account the asymmetry of the peaks by parameter β. The further the relaxation peak is shifted to lower *T*, the faster the Li exchange process inducing spin-lock spin–lattice relaxation. Therefore, Li diffusion, as seen by NMR, is increasing in the following order: Li_6PS_5I < Li_6PS_5Br < Li_6PS_5Cl (see also c). (c) R_1 and $R_{1\rho}$ of Li_6PS_5I; at 160 K Li_6PS_5I reversibly transforms into its low-*T* phase. At this temperature the rates R_1 show a jump toward lower values; the $R_{1\rho}$ rates sharply decay with an activation energy of 0.44 eV. The unfilled symbols in (a–c) show rates measured with an NMR probe designed for experiments at cryogenic temperatures; the filled symbols refer to data which were acquired with a standard probe.

with temperature and characteristic diffusion-induced rate peaks show up. We recognise that R_1 passes through well-defined maxima as has been found by some of us in an earlier study on the ion dynamics in Li_6PS_5Br.[15] At the temperature T_{max}, where R_1 reaches its maximum value, the motional correlation rate $1/\tau_c$ is given by $\tau_c\omega_0 \approx 1$. $1/\tau_c$ is identical within a factor of two to the Li jump rate $1/\tau$.[61,65] The same holds for $R_{1\rho}$, for which the maximum condition is $\omega_1\tau \approx 0.5$.[61,65] As ω_0 and ω_1 differ by more than three orders of magnitude, the SLR NMR experiments, when taken together, are able to sense motional processes covering a large time scale.[67,68]

We notice that the rate peak of Li_6PS_5Br shows up at T_{max} = 286 K. The peak is asymmetric and we used a Lorentzian-type (BPP-type)[62,69] spectral density function $J(\omega_0) \propto R_1$ of the form[70]

$$J(\omega_0) \propto \frac{\tau_c}{1 + (\omega\tau_c)^\beta} \tag{4}$$

to approximate its shape. Eqn (4) holds for 3D diffusion; $J(\omega_0)$ is the Fourier transform of the underlying motional correlation function $G(t')$. If $G(t')$ is a single exponential, β in $J(\omega_0)$ takes a value of 2. For a 3D diffusion process, at high temperatures, *i.e.*, if $\tau_c\omega_0 \ll 1$, eqn (4) yields $J \propto \tau_c$; in the limit $\tau_c\omega_0 \gg 1$, that is, on the low-T side of the rate peak, we have $J \propto \tau^{-1}\omega_0{}^{-\beta}$ $(1 < \beta \leq 2)$. While we expect $\beta = 2$ for uncorrelated motion,[61,62,69,71] asymmetric peaks are often found for structurally complex ion conductors[15,71–73] whose dynamic processes are affected by correlation effects because of both disorder and strong Coulomb interactions of the moving ions.[71] For such materials the activation energies for short-range and long-range processes might largely differ.[62] In general, β can also be related to a distribution width of motional correlation times; in this sense it has a similar meaning to the exponent in the Cole–Davidson spectral density function used to approximate asymmetric rate peaks.[74–76]

Here, the analysis of the rate peak of Li_6PS_5Br with eqn (4) yields an activation energy $E_{a,NMR}$ of 0.213 eV, which is in perfect agreement with earlier findings for this compound.[15,50] As mentioned above, the parameter β describes the deviation from symmetric behaviour ($\beta = 2$). β turned out to be $\beta \approx 1.5$,[65] which gives rise to a much lower activation energy $E_{a,low}$ on the low-T side of the peak. In this regime, characterised by $\tau_c\omega_0 \ll 1$, short-range or localised ion dynamics in double-well potentials, including also highly correlated forward–backward jumps, are sensed by R_1.[61] The activation energy of the low-T flank is given by 0.10 eV, which is in very good agreement with that seen by $\rho'(\omega)$. Localised intracage jump processes involving the 48h and 24g sites in Li_6PS_5Br could be mainly responsible for spin–lattice relaxation in this region, as has been precisely calculated (0.11 eV) by De Klerk *et al.*[50] The higher activation energy $E_{a,high}$(=$E_{a,NMR}$) seen in the limit $\tau_c\omega_0 \ll 1$ might, however, additionally be affected by 48h–48h jumps. Usually in this regime, in which many jump processes occur during one Larmor precession of the spin, $E_{a,NMR}$ should be comparable with $E_{a,DC}$ (0.296 eV) or $E_{a,\rho}$ (0.250 eV).[61] $E_{a,DC}$ could be influenced by g.b. effects; here, $E_{a,NMR} < E_{a,\rho}$ shows that the number of jump events sensed by NMR, which should not necessarily include all types of jumps needed for long-range diffusion, is sufficient to generate a full R_1 peak.

Table 1 Results of the individual BPP-fits used to analyse the ^{7}Li NMR R_1 and $R_{1\rho}$ peaks of the three argyrodite samples Li_6PS_5X (X = Cl, Br, I). For comparison, the activation energies obtained from the low-T flank, $E_{a,low}$, are also included

	Li_6PS_5Cl[a]	Li_6PS_5Br[a]	Li_6PS_5I[b]
β	1.53(2)	1.48(2)	1.92(1)
E_a	0.320(1) eV	0.213(1) eV	0.198(1) eV
$E_{a,low}$	0.170(4) eV	0.102(5) eV	0.182(5) eV
τ_0	$1.3(5) \times 10^{-14}$ s	$2.3(5) \times 10^{-13}$ s	$8.2(5) \times 10^{-13}$ s
β_ρ	1.54	1.41	—
$E_{a,\rho}$	0.248(9) eV	0.201(9) eV	0.137(3) eV
$E_{a,low}$	0.134(1) eV	0.083(1) eV	—
$\tau_{0,\rho}$	$9.5(5) \times 10^{-13}$ s	$3.3(1) \times 10^{-12}$ s	—

[a] The best $R_{1\rho}$ fit is obtained if we replace $\omega_1/2\pi$ = 20 kHz by a slightly higher effective locking frequency ω_{eff} that also takes into account local magnetic fields. For Li_6PS_5Cl several runs of the global fit procedure yields $\omega_{eff} = 1.68 \times \omega_1$; for Li_6PS_5Br ω_{eff} is given by $\omega_{eff} = 1.41 \times \omega_1$. [b] Li_6PS_5I undergoes a phase transition at 160 K; thus, no β_ρ can be observed. The symmetric rate peak ($\beta \approx 2$) agrees with the ordered anion sublattice as suggested by XRPD, see above.

A very similar behaviour is found for Li_6PS_5Cl. The corresponding rate peak is shifted toward higher temperature revealing that faster ion dynamics is present in Li_6PS_5Br. In agreement with conductivity spectroscopy and our $\rho'(\omega)$ analysis, for Li_6PS_5Cl higher activation energies ($E_{a,high}$ = 0.32 eV, $E_{a,low}$ = 0.17 eV) than those seen for the Br analogue were found. Although $E_{a,high}$ = 0.32 eV perfectly agrees with $E_{a,\rho}$, see Fig. 10, and calculated values,[35] it is higher than expected from $R_{1\rho}$ NMR in the limit $\tau_c\omega_1 \ll 1$ (0.248 eV). Furthermore, the shapes of the $R_1(1/T)$ peaks of the two compounds are very similar. Obviously, similar (local) jump processes influence the NMR rates. In Table 1 an overview of the parameters is given obtained from the analysis with individual BBP-type spectral densities for each peak.

Exactly the same trend is seen when we look at the $R_{1\rho}(1/T)$ peaks of the two compounds, which are shown in Fig. 11b. These have been, independently of the R_1 experiments, also parameterised with Lorentzian-shaped spectral density functions. The activation energies of the peak of Li_6PS_5Br (0.201 eV, 0.083 eV) match with those reported earlier[15] also including calculated values.[50] They also agree with those from the R_1 peak. Here, $R_{1\rho}(1/T)$ of Li_6PS_5Br turned out to be much smaller that that reported by Yu *et al.*;[77] most likely, the difference has to be looked for in the preparation conditions such as milling steps and annealing procedures.

In Fig. 12 so-called joint fits[65] of the two types of NMR experiments, R_1 and $R_{1\rho}$, are shown. For the joint fits the parameters $E_{a,NMR}$ and $\tau_0{}^{-1}$, which is the pre-factor of the Arrhenius equation of $\tau_c{}^{-1}$, have been linked to each other. The best fit is obtained if we use two independent values for β and if we replace ω_1 by effective frequencies $\omega_{1,eff}$, also taking into account local magnetic fields.[73] To estimate the latter, we did not fix ω_1 and looked at how the quality of the fit changes if it is a free parameter. Only a slight change of ω_1 was necessary giving rise to $\omega_{eff} \approx 1.5 \times \omega_1$. A successful joint fit shows that the same overall diffusion processes govern the peaks R_1 and $R_{1\rho}$. The results of our joint fits are shown in Table 2.

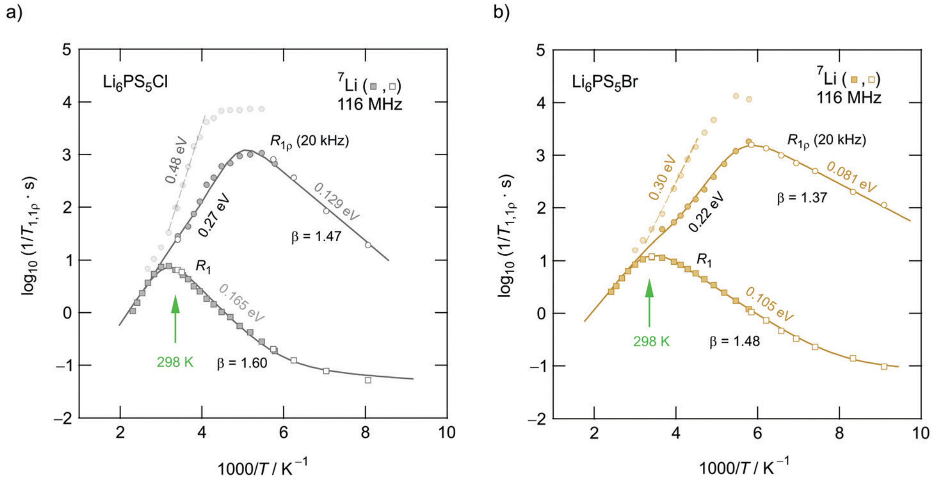

Fig. 12 Arrhenius plot of the ^{7}Li NMR relaxation rates R_1 and $R_{1\rho}$ of (a) Li$_6$PS$_5$Cl and (b) Li$_6$PS$_5$Br measured in the laboratory frame of reference (116 MHz) and in the rotating frame of reference (20 kHz, nominal locking frequency). The solid lines represent the global fit based on a modified BPP model that takes into account peak asymmetries by the parameter $\beta_{(\rho)}$. The fastest Li diffusion is found for Li$_6$PS$_5$Br with the peak maxima showing up at 286 K and 168 K, respectively. The second $R_{1\rho}$ relaxation process, most likely also influenced by spin–spin relaxation to a certain degree, is indicated, too. As mentioned before (see Fig. 11), the open symbols represent rates that were measured with an NMR probe designed for experiments at cryogenic temperatures; the filled symbols show rates which were acquired with the standard probe.

Table 2 Results of the overall fit used to jointly parameterise the ^{7}Li NMR R_1 and $R_{1\rho}$ peaks of Li$_6$PS$_5$Br and Li$_6$PS$_5$Cl. E_a agrees well with the results if we analyse the peaks individually. For comparison, results for Li$_6$PS$_5$I taken from Table 1 are also included

	$E_{a,\text{NMR}}$	C	$\beta_{(\rho)}$	τ_0
Li$_6$PS$_5$Cl				
R_1	0.273(5) eV	$3.5(5) \times 10^9$ s^{-2}	1.60(1)	$4.9(4) \times 10^{-14}$ s
$R_{1\rho}$		$3.1(5) \times 10^{10}$ s^{-2}	1.47(1)	
Li$_6$PS$_5$Br				
R_1	0.218(1) eV	$5.6(7) \times 10^9$ s^{-2}	1.48(1)	$2.0(2) \times 10^{-13}$ s
$R_{1\rho}$		$3.3(9) \times 10^{10}$ s^{-2}	1.47(1)	
Li$_6$PS$_5$I[a]				
R_1	0.198(1) eV	$1.1(4) \times 10^{10}$ s^{-2}	1.92(1)	$8.2(9) \times 10^{-13}$ s
$R_{1\rho}$	0.137(3) eV	—	—	—

[a] The best global fits are obtained if we replace ω_1 by the effective locking frequencies $\omega_{\text{eff}} = 1.68 \times \omega_1$ (Li$_6$PS$_5$Cl) and $\omega_{\text{eff}} = 1.41 \times \omega_1$ (Li$_6$PS$_5$Br). The coupling constant C, which is the amplitude of the rate peak, $J(\omega_0) = C\tau_c/(1 + (\omega\tau_c)^\beta)$, turns out to be on the order of 10^9 to 10^{10} s^{-2}.

The activation energies $E_{a,\text{NMR}}$ (=$E_{a,\text{high}}$) obtained fulfill the relationship

$$E_{a,\text{low}} = (\beta_{(\rho)} - 1)E_{a,\text{high}}. \quad (5)$$

$\beta_{(\rho)} < 2$ points to correlated Li$^+$ motion and indicates a subquadratic dependence of the diffusion-induced SLR NMR rates in the low-T limit $\tau_c\omega_{0(1)} \gg 1$. Our results are in good agreement with those of Epp *et al.* as well as Rao *et al.*[15,35] We clearly see that correlation effects such as structural disorder and Coulomb interactions[71] have a larger effect on the cation dynamics in Li$_6$PS$_5$Br than in Li$_6$PS$_5$Cl.

Considering the overall constants C obtained from the joint fits, they reveal that both dipolar and electric quadrupolar interactions govern the diffusion-induced SLR NMR rates. Estimating C_{dipolar} with the help of the rigid lattice line width for Li$_6$PS$_5$Br and Li$_6$PS$_5$Cl would underestimate C to be on the order of 10^{10} s^{-2}.[46] As we will discuss below, for Li$_6$PS$_5$Br quadrupolar interactions have been identified to greatly influence longitudinal relaxation.[15]

Interestingly, a very close look at the $R_{1\rho}$ magnetization transients revealed that they contain a minor magnetization component that leads to activation energies of 0.484 eV (Li$_6$PS$_5$Cl) and 0.298 eV (Li$_6$PS$_5$Br); the corresponding $R_{1\rho}$ rates are included in Fig. 12. We cannot exclude that these rates are to a certain degree also influenced by spin–spin relaxation. Obviously, the rates sense long-range Li jump processes characterised by higher activation energies. The intercage jumps might contribute to this type of magnetic relaxation, too.

For X = Cl and Br, if we consider activation energies, $T_{\max}$, β and β_ρ, the ^{7}Li SLR NMR data reveal the same trend for the ion dynamics as seen by the conductivity and $\rho'(\omega)$. Li$_6$PS$_5$Br shows fast ion dynamics and the lowest activation energies. For Li$_6$PS$_5$Cl we witness slightly higher activation energies; simultaneously, the peaks shift toward higher temperature. For Li$_6$PS$_5$I, on the other hand, significant differences show up (see the next section).

The NMR rate peaks of Li$_6$PS$_5$I, remembering its low σ_{DC} conductivity of 10^{-6} S cm^{-1} at ambient temperature, are expected to show up at temperatures much higher than 320 K. We would expect much higher activation energies, at least similar to or higher than those found for Li$_6$PS$_5$Cl. Surprisingly, the R_1 rate peak of Li$_6$PS$_5$I shows up at a temperature highly comparable to that of Li$_6$PS$_5$Cl *viz.* at $T_{\max}$ = 329 K, see Fig. 11a. In stark contrast to our expectation, NMR does not point to slower Li$^+$ diffusion. Hence, in Li$_6$PS$_5$I the same fast (local) jump processes are present as in their parent compounds.[35,40,50] Here, we anticipate that the Li ions in Li$_6$PS$_5$I, with its ordered anion sublattice, have access to the same rapid intracage jump processes. According to NMR the barriers have to be characterised by an activation energy of 0.2 eV. Obviously, only intracage jump processes in Li_6PS_5I are sufficient to produce a full $R_1(1/T)$ peak, see the discussion above.

As expected for a material with an ordered anion lattice such as Li_6PS_5I and without severe influences of motional correlation effects, an almost symmetric rate peak $R_1(1/T)$ (β = 1.92($\approx\beta'$)) is obtained for Li_6PS_5I. The same shape was seen in $\rho'(\omega)$. Interestingly, an even lower activation energy determines $R_{1\rho}(1/T)$, see Fig. 11c: in the limit $\tau_c\omega_1 \ll 1$ the rates follow an Arrhenius line whose activation energy $E_{a,high}$ is given by only 0.137 eV. This value is remarkably similar to a cage-like local pathway studied by Rao and Adams (0.15 eV) who used a bond valence approach to investigate the Li ion dynamics in Li_6PS_5I. Our experimental value also coincides with that of Pecher *et al.*[40] (0.14 eV) who studied the local ion dynamics by molecular dynamics simulations.

The amplitude $(R_1)_{max}$ of the $R_1(1/T)$ rate of Li_6PS_5I turned out to be higher that that of the peaks belonging to Li_6PS_5Cl and Li_6PS_5Br. This could be because of stronger heteronuclear Li–X interactions and the fact that Li ions on the distorted 24g sites give rise to stronger dipolar and electric quadrupolar couplings constants. These are lowest for the Li_6PS_5Cl compound. In general, $(R_1)_{max}$ is proportional to the square of the magnetic dipolar or electric quadrupolar coupling constant.[75,78,79] If we use an electric quadrupole constant of at least 50 kHz, as has been estimated for Li_7PS_6,[46] we obtain $(R_1)_{max} \approx 2\ s^{-1}$ yielding $\log_{10}((R_1)_{max}/s) \approx 0.3$, showing that for Li_6PS_5Cl both dipolar and electric quadrupolar interactions play a role in determining the relaxation mechanism. For Li_6PS_5Br we showed *via* comparative ^7Li and ^6Li SLR NMR measurements that quadrupole fluctuations greatly affect the overall spin–lattice relaxation.[15]

Coming back to the temperature dependence of the SLR NMR rates of Li_6PS_5I, we see that at higher temperatures than ambient the rates $R_{1\rho}$ are increasingly governed by R_1, which produces an apparent maximum at *ca.* 330 K. Unfortunately, the peak maximum of $R_{1\rho}(1/T)$ cannot be detected as Li_6PS_5I undergoes a phase transition at 160 K;[31,39,40,49] see the abrupt change in $R_{1\rho}$ in Fig. 11c. The ion dynamics in the low-T (LT) phase is characterised by a much higher activation energy of 0.44 eV. Below 160 K the rates R_1 are no longer induced by diffusive Li jump processes.

To explain the evident differences between the results from conductivity measurements and nuclear spin relaxation in Li_6PS_5I we anticipate that the fast diffusion Li processes in the I compound are not interconnected to give rise to long-range, through-going ion transport. As has been pointed out in detail by Wagemaker and coworkers, and first mentioned by Rao and Adams,[35] the jump probability between two rings in Li_6PS_5I is very low.[50] Intercage jump processes with higher activation energies lead to poor ion transport in Li_6PS_5I. On a shorter length scale, however, the same structural motifs in Li_6PS_5X cause very similar NMR rate peaks. Anion disorder, taking advantage of anions with radii that do not differ much to that of S^{2-}, switches on the intercage exchange processes, making Li_6PS_5Br a fast ion conductor. This design principle causes the overall activation energy to increase in the following order: $Li_6PS_5Br < Li_6PS_5Cl < Li_6PS_5I$.

To verify whether some intragrain translational processes needed for long-range diffusion in Li_6PS_5I are indeed missing or governed by higher activation energies we carefully looked at the $R_{1\rho}$ transients and recorded ^7Li NMR line shapes over a broad temperature range (Fig. 13). Interestingly, the above-mentioned slow magnetization component seen for Li_6PS_5Cl and Li_6PS_5Br (Fig. 12) is missing for the I compound. Furthermore, the intercage jumps are expected to contribute to the averaging of homonuclear (Li–Li) dipole–dipole interactions. If missing at low temperatures, for Li_6PS_5I the change in line width $\Delta\nu$ should occur in two steps. Full averaging is expected at temperatures for which the intercage exchange rate reaches sufficiently high values on the order of some kHz. Indeed, whereas for Li_6PS_5Br and Li_6PS_5Cl the ^7Li NMR line width continuously decreases with temperature revealing typical narrowing curves (Fig. 13a), that of Li_6PS_5I is different.

For Li_6PS_5Br and Li_6PS_5Cl the extreme narrowing regime is already reached at 250 K ($\nu_\infty \approx$ 300 Hz); the final line width is caused by external field inhomogeneities. In contrast to the situation observed for Li_6PS_5Br and Li_6PS_5Cl, at 250 K the ^7Li NMR line of Li_6PS_5I is still relatively broad and shows a width of ν = 2.2 kHz. At 350 K it finally reaches ν_∞. Thus, for Li_6PS_5I full averaging of the NMR line width is shifted by ΔT = 100 K toward higher T. Most likely, the latter step corresponds to intercage ion dynamics which are governed by a larger activation barrier. Hence, it is clear from NMR motional narrowing data that in Li_6PS_5I a much slower process kicks in only at higher T. The fact that $\Delta\nu$ of Li_6PS_5I and Li_6PS_5Cl is very similar, at least at temperatures just above the phase transition, shows that mainly fast intracage jump processes are responsible for the narrowing seen in this T range. Differences show up, however, if we consider the rotating-frame spin–lattice relaxation rates, see above. The activation energies of the two samples differ by *ca.* 0.11 eV. Interestingly, the $R_{1\rho}(1/T)$ peak of Li_6PS_5I is expected at a similar temperature to that of Li_6PS_5Br (0.20 eV), again pointing to very fast intracage jump processes in the iodide compound. Most likely, so-called doublet-jump processes[50] have to be considered to explain this feature, see below.

Unfortunately, we cannot probe the rigid-lattice line width ν_0 of the Li_6PS_5I compound because of the phase transition that occurs at 160 K.[31,39,40,49] For both Li_6PS_5Br and Li_6PS_5Cl the value of ν_0 is very similar; ν_0 turned out to be *ca.* 6.1 kHz. Therefore, the magnetic dipolar Li–Li interactions, which are determined by the Li–Li distances, are almost the same in the two compounds. The inflexion point of the motional narrowing curve of Li_6PS_5Br is located at T = 150 K (Fig. 13a). $R_{1\rho}(1/T)$ tells us that at this temperature the motional correlation rate τ_c^{-1} ($\approx 2\omega_1$) should be on the order of $2.51 \times 10^5\ s^{-1}$. This value clearly exceeds ν_0 and causes full averaging of the spin–spin interactions in this T range. The changes of the corresponding ^7Li NMR lines are shown in Fig. 13b. Li_6PS_5Br shows one of the lowest onset temperatures seen by NMR motional line narrowing; already at 86 K the shape of the NMR line starts to change as a result of rapid Li^+ self-diffusion.[15] This observation excellently agrees with results from density functional theory molecular dynamics simulations.[50]

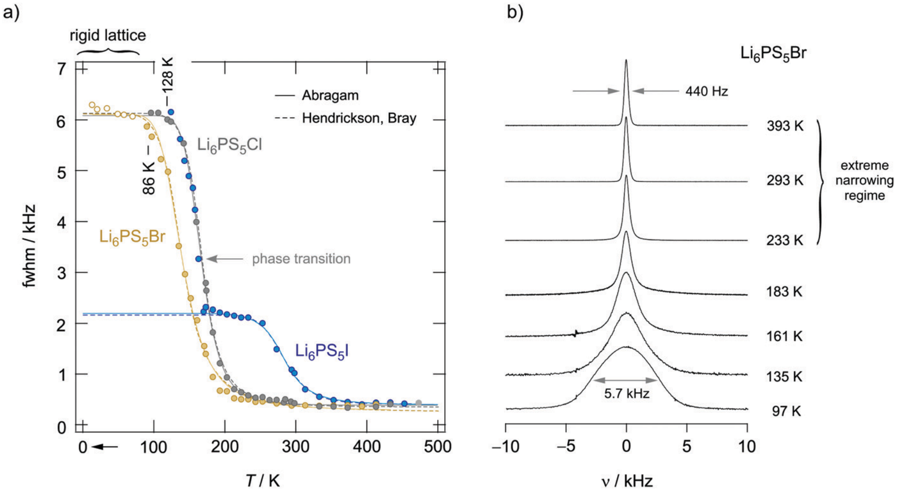

Fig. 13 (a) Temperature dependence of the ^{7}Li NMR line widths (FWHM = full width at half maximum) of the aryrodites Li_6PS_5X (X: Cl, Br and I). Some of the data points referring to Li_6PS_5Br and measured at temperatures lower than 80 K were taken from Epp *et al.*;[15] they perfectly complement the results of the sample studied here. Line widths $\Delta\nu_r(T)$ of Li_6PS_5Br start to narrow at temperatures as low as 86 K indicating ultrafast hopping processes that average homonuclear dipole–dipole interactions being responsible for the rigid lattice line width $\Delta\nu_r \approx 6.1$ kHz. Li diffusion in the compound with Cl is slightly slower as the onset of line narrowing is shifted toward higher *T*. The line of $\Delta\nu_r(T)$ of Li_6PS_5I narrows in steps of two. At $T < 160$ kHz it indicates dipole averaging in the low-*T* phase. Because inter-ring jump processes are absent, the line does not reach its extreme value at a temperature comparable to that of Li_6PS_5Br and Li_6PS_5Cl. Higher temperatures are necessary to obtain a fully narrowed ^{7}NMR line. Lines represent fits according to the models of Hendrickson and Bray (dashed lines) and Abragam (solid lines). (b) ^{7}NMR line shapes of Li_6PS_5Br recorded at the temperatures indicated; the line transforms from a Gaussian shape at low *T* to a Lorentzian one at elevated temperatures.

Extracting quantitative information from NMR motional line narrowing is always fraught with difficulties.[80] Abragam[81] and Hendrickson and Bray[82,83] introduced models to use the change in line widths to deduce activation energies for the hopping process behind. There is still debate over whether these models are accurate enough for this purpose. Hence, we should not over-interpret the results but regard them as estimates. The dashed lines in Fig. 13 refer to the following relationships[82]

$$\Delta\nu(T) = \Delta\nu_0\left\{1 + [(\Delta\nu_0/B) - 1]\exp\left(-\frac{E_{\mathrm{a,HB}}}{k_{\mathrm{B}}T}\right)\right\}^{-1} + \nu_\infty \quad (6)$$

$\Delta\nu(T)$ is the line width of the central transition at a given temperature and B is a parameter that is related to the number of thermally activated ions.[82] The final line width ν_∞ is determined by the inhomogeneities of the external magnetic field B_0. Another possibility to deduce activation energies is given by the formalism of Abragam[81] (see the solid line in Fig. 13):

$$\Delta\nu^2(T) = \Delta{\nu_0}^2\frac{2}{\pi}\arctan\left[\alpha\Delta\nu(T)\tau_\infty\exp\left(\frac{E_{\mathrm{a,A}}}{k_{\mathrm{B}}T}\right)\right] + \Delta{\nu_\infty}^2 \quad (7)$$

α is a fitting parameter, here chosen to be 1. τ_∞ is the pre-factor of the underlying Arrhenius law of the correlation time τ_c. With the Abragam fit we obtained activation energies $E_{\mathrm{a,A}}$ of 0.06 eV (Li_6PS_5Br), 0.11 eV (Li_6PS_5Cl) and 0.23 eV (Li_6PS_5I), respectively. Typically, the formalism of Hendrickson and Bray yields somewhat higher activation energies; here, we found $E_{\mathrm{a,HB}} = 1.6 \times E_{\mathrm{a,A}}$, see Table 3. Interestingly, although line narrowing is expected to be sensitive to long-range ion dynamics which can fully average all dipolar interactions, the activation energies $E_{\mathrm{a,A}}$ and $E_{\mathrm{a,HB}}$ are remarkably similar to those governing the low-*T* flank of the $R_1(1/T)$ peaks, see also Table 3.

Table 3 Activation energies obtained when analysing the motional narrowing curves shown in Fig. 13. We used the Abragam (A) and Hendrickson–Bray (HB) formalism to extract activation energies; the error is in the last digit. For comparison, activation energies describing the slopes of the $R_1(1/T)$ peaks in the limit $\tau_c\omega_0 \gg 1$ are also shown

	$E_{\mathrm{a,A}}$ (eV)	$E_{\mathrm{a,HB}}$ (eV)	E_{a} (low-T flank) (eV)
Li_6PS_5Cl	0.11(1)	0.18(2)	0.17(4)
Li_6PS_5Br	0.06(1)	0.09(1)	0.10(4)
Li_6PS_5I	0.23(1)	0.38(2)	0.18(5)

Finally, we will quantitatively compare jump rates τ^{-1} from NMR with electrical relaxation rates from impedance and conductivity spectroscopy. Using the Nernst–Einstein equation[84] we can convert σ' into diffusion coefficients and, thus, jump rates. The easiest way, being also independent of any relaxation model, is to determine jump rates τ^{-1} at the temperatures where the NMR relaxation rate peaks show up. With the conditions $\tau_c\omega_{1(\rho)} = 1(0.5)$, valid at T_{max}, and the jump distances ℓ obtained from XRD we estimated diffusion coefficients according to the Einstein–Smoluchowski relation[84] for 3D diffusion

$$D_{\mathrm{NMR}} = \frac{\ell^2}{6\tau}. \quad (8)$$

For ℓ we used the jump distance of the 48h–48h jump process, which is assumed to be the slowest one. The results are listed in Table 4. At T_{max} the jump rate turned out to be on the order of 1.36×10^{-9} s^{-1}. As an example, the mean residence time of the Li ions in Li_6PS_5Br at 286 K is on the order of 1 ns only. Such a short residence time, which is already reached below room temperature, corresponds to ionic conductivities on the order of 10^{-3} to 10^{-2} S cm^{-1}.

Table 4 Results of the diffusion coefficient D. τ was calculated from the $R_1(1/T)$ rate peak measurements performed at 116 MHz

	ℓ/Å	$T_{\max}(R_1)$/K	D_{NMR}/cm^2 s^{-1}	n_{Li}/m^{-3}
Li_6PS_5Cl	2.34	316	6.7×10^{-8}	6.3×10^{27}
Li_6PS_5Br	2.41	286	7.1×10^{-8}	6.0×10^{27}
Li_6PS_5I	2.66	329	8.6×10^{-8}	5.8×10^{27}

For ℓ we used the 48h–48h distance, which is the longest jump distance in Li_6PS_5Br, when we consider cation hopping processes near the regularly occupied Li sites.

Using structural data from our Rietveld analysis we also estimated the charge carrier density n_{Li} in Li_6PS_5Br. n_{Li}, which is on the order of 10^{27} m^{-3}, is needed to convert D_{NMR} into conductivities expected at or near $T_{\max}$. Disregarding any correlation effects for our estimation of σ_{NMR}, the following relation holds[11]

$$\sigma_{\mathrm{NMR}} = \frac{e^2 \cdot n}{k_{\mathrm{B}}T} D_{\mathrm{NMR}} = \frac{e^2 \cdot n_{\mathrm{Li}} \cdot \ell^2}{6k_{\mathrm{B}}T} \cdot \frac{1}{\tau}. \tag{9}$$

where e denotes the elementary charge. Here, a residence time τ of 1 ns results in conductivities of the order of 2 mS cm^{-1}. In Table 5 the estimated results from NMR are compared with those measured by conductivity spectroscopy. Assuming no correlation effects or other influences for this estimation means that H_R/f in $D_{\mathrm{NMR}} = (H_R/f)D_\sigma$ is approximated by $H_R/f = 1$; while H_R denotes the Haven ratio connecting the tracer diffusion coefficient D_{tr} with D_σ, the correlation factor f links D_{NMR} with D_{tr}.[11]

While good agreement is seen for σ_{NMR} and σ_{DC} of Li_6PS_5Br, we have to notice a somewhat larger difference for the Cl compound. In general, conductivities indirectly deduced from NMR should be regarded as estimates because relaxation NMR and conductivity spectroscopy sense different kinds of motional correlation functions. Agreement over a large temperature is only obtained if both techniques are sensitive to the same diffusion process and the same correlation function.[51]

As expected, for Li_6PS_5I the values listed in Table 5 differ by three orders of magnitude. Whereas σ_{DC} is mainly governed by successful jump processes resulting in long-range ion transport, σ_{NMR} reflects short-range ion dynamics. The difference can easily be explained by the fact that in Li_6PS_5I the intercage jump processes are less probable; these processes hinder the ions in long-range diffusion. Note that the comparison in Table 5 only refers to $T \approx T_{\max}$ at which the NMR peaks show up. Comparing dynamic parameters over the full temperature range will show deviations between nuclear spin relaxation and conductivity spectroscopy as the techniques deliver different activation energies in the present case. Such a comparison is presented in Fig. 14. Squares represent jump rates obtained at the NMR rate peaks; at $T \to 0$ we have indicated the pre-factors of the Arrhenius lines.

Table 5 Estimated conductivity values (σ_{NMR}) from NMR data. For comparison, the measured values σ_{DC} are also listed

	σ_{NMR}/mS cm^{-1}	σ_{DC}/mS cm^{-1}
Li_6PS_5Cl	2.46 (316 K)	9.00 (313 K)
Li_6PS_5Br	2.78 (286 K)	2.20 (293 K)
Li_6PS_5I	2.80 (329 K)	8.60×10^{-3} (333 K)

In Fig. 14a τ_{NMR}^{-1} as deduced from the joint fits of Li_6PS_5Cl and Li_6PS_5Br are shown. The line belonging to Li_6PS_5I refers to the R_1 rates only. First of all, we notice a correlation between $E_{\mathrm{a,NMR}}$ and the pre-factor τ_0^{-1} (see also Table 2). The decrease in $E_{\mathrm{a,NMR}}$, which changes from 0.273 eV to 0.218 eV and further to 0.198 eV (R_1 of Li_6PS_5I), is accompanied by a decrease in τ_0^{-1}. The attempt frequency τ_0^{-1} decreases by a factor of 80 when going from Li_6PS_5Cl to Li_6PS_5I. This small variation either reflects a decrease in phonon frequencies or a change in migration entropy ΔS of the ions as $\tau_0^{-1} = \nu_{\mathrm{p},0}\exp(\Delta S/k_{\mathrm{B}})$. Phonon frequencies, to which $\nu_{\mathrm{p},0}$ is proportional, usually take values on the order of 10^{12} to 10^{15} s^{-1}. As discussed above, for Li_6PS_5I a decrease in migration entropy is reasonable because of the ordered anion sublattice. The decrease in $E_{\mathrm{a,NMR}}$ reflects the increase in anion polarizability (I > Br > Cl), which should, apart from effects due to disorder, also lead to lower hopping barriers. This trend for $E_{\mathrm{a,NMR}}$ is at least valid for the elementary Li^+ jumps seen by NMR. If we include τ_σ^{-1} values obtained by transforming σ_{DC} into hopping rates after eqn (9), we notice that good agreement is only seen at temperatures around $T_{\max}$, see Fig. 14a and b. Clearly, the fact that $E_{\mathrm{a,NMR}} \neq E_{\mathrm{a,DC}}$ leads to deviations at temperatures $T \lessgtr T_{\max}$. For comparison, in Fig. 14b hopping rates from $\rho'(T)$ have also been included.

The pre-factors of the Arrhenius lines referring to τ_σ^{-1} estimated from σ_{DC} also vary with X. While we cannot see any large difference between $\tau_{0,\sigma}^{-1}$ from Li_6PS_5I and Li_6PS_5Br as mentioned above, we see that $\tau_{0,\sigma}^{-1}$ of the Cl-compound is much higher than expected. This increase is caused by a change in slope of σ_{DC} at a temperature slightly below 400 K; it is also seen for Li_6PS_5I. Below 400 K the ionic conductivity σ_{DC} (as well as τ_σ^{-1}) follows an Arrhenius law with an activation energy very similar to that of Li_6PS_5Br (0.273 eV). As σ_{DC} of Li_6PS_5Br and Li_6PS_5Cl almost coincide in this T range, also the corresponding pre-factors $\tau_{0,\sigma}^{-1}$ would be the same. Here, the fact that $\tau_{0,\sigma}^{-1}$ of Li_6PS_5Cl is larger than that of Li_6PS_5Br originates the kink in the Arrhenius line causing $\sigma_{\mathrm{DC}}T(1/T)$ to be characterised by an activation energy (0.396 eV) much larger than that in the low-T range. Obviously, another Li^+ diffusion process, being characterised by an activation energy larger than 0.3 eV, contributes to τ_σ^{-1} of Li_6PS_5Cl.

Such an additional process, which we assume could stem from an ordered Li sublattice in Li_6PS_5Cl, has been seen by $R_{1\rho}$, see Fig. 12. The $R_{1\rho}$ magnetization transients of Li_6PS_5Cl are characterised by a second decay process that is thermally activated by 0.48 eV. The same feature is also seen for Li_6PS_5Br with both a disordered anion structure and Li^+ sublattice. The corresponding activation energy of 0.30 eV (see Fig. 12) is, however, very similar to that of $\sigma_{\mathrm{DC}}T(1/T)$. This similarity thus gives rise to no increase in $\sigma_{\mathrm{DC}}T$ above $T \approx 400$ *K*.

The pre-factors seen by conductivity spectroscopy, especially those of Li_6PS_5Cl, clearly represent mean values. In materials with several diffusion processes taking place in parallel, each process needs to be characterised by its individual pre-factor.

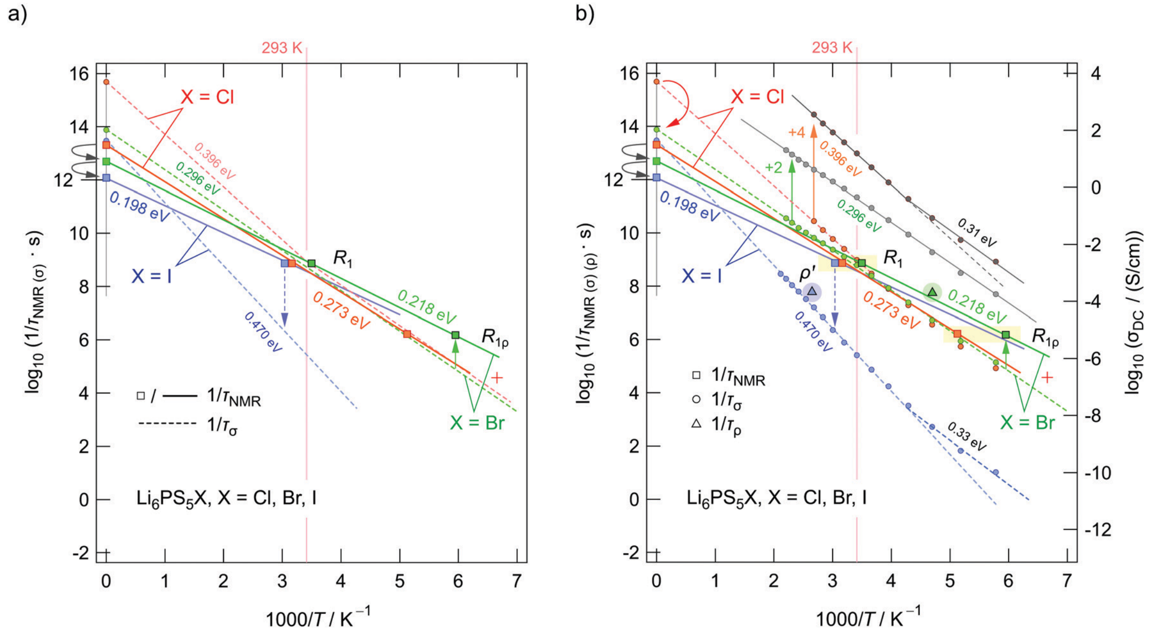

Fig. 14 Arrhenius plot of the jump rates deduced from the ^{7}Li NMR rate peaks shown in Fig. 11c, 12a and (b). (a) Squares represent either pre-factors or jump rates at the maxima of the peaks. Solid lines represent the Arrhenius lines according to the joint fits. Dashed lines indicate the position of τ_σ^{-1}, *i.e.*, estimated from σ_{DC}. (b) The same data points as in (a) but with τ_{DC}^{-1} included as data points. The lines referring to Li_6PS_5Cl and Li_6PS_5Br have been shifted by a factor of +4 (+2) (on the log scale) to illustrate the kink seen in $\tau_{DC}^{-1}(1/T)$ for Li_6PS_5Cl. It is absent for Li_6PS_5Br. Electrical relaxation rates τ_ρ^{-1} from our $\rho'(1/T)$ analyses have been included as well. The vertical arrow drawn with a dashed line indicates the large difference in jump rates seen for Li_6PS_5I. The arrows near the ordinate illustrate the change in pre-factors. See the text for further explanation.

Table 6 Activation energies as deduced from the various methods applied here to investigate the ion dynamics in Li_6PS_5X by conductivity spectroscopy and NMR relaxometry

	Li_6PS_5Cl (eV)	Li_6PS_5Br (eV)	Li_6PS_5I (eV)
σ_{DC}	0.396(3)	0.296(2)	0.470(5)
ρ', high-*T* flank[a]	0.321(3)	0.250(3)	0.347(7)
ρ', low-*T* flank[a]	0.153(2)	0.115(9)	0.305(2)
M''	—	—	0.349(5)
R_1, high-*T* flank[a]	0.320(1)	0.213(1)	0.198(1)
R_1, low-*T* flank[a]	0.170(4)	0.102(4)	0.182(5)
$R_{1\rho}$, high-*T* flank[a]	0.248(9)	0.201(9)	0.137(3)
$R_{1\rho}$, low-*T* flank[a]	0.134(1)	0.083(1)	—
R_1 (global fit)[b]	0.273(5)	0.218(1)	—
	(0.165(8))	(0.105(4))	—
$R_{1\rho}$ (global fit)[b]	0.273(5)	0.218(1)	—
	(0.129(7))	(0.081(4))	—

[a] The values referring either to the high-*T* or to the low-*T* flank were obtained by a line fit. [b] Results from the global fit analysis are obtained by linking E_a and τ_0^{-1} of the individual relaxation rate peaks. Values in brackets refer to the low-*T* flanks of the global fit.

In the case of ^{7}Li NMR, which is primarily sensitive to the elementary jump processes between 24g and 48h, we see a slight increase in the pre-factor when going from X = I to X = Cl (see above). The change in τ_0^{-1} is, however, small as compared to the drastic decrease in $\sigma_{DC}T(1/T)$ seen for Li_6PS_5I. Hence, the increase in overall migration enthalpy for Li_6PS_5I, for which the intercage diffusion process is characterised by a high hopping barrier, turned out to be mainly responsible for its poor ionic conductivity. On shorter length scales, Li ion hopping in Li_6PS_5I, with its ordered anion sublattice, is as fast as in Li_6PS_5Br. This result is in perfect agreement with the pioneering calculations by Rao and Adams as well as the in-depth study presented by De Klerk *et al.*[50] They already pointed out, as mentioned above, that for Li_6PS_5I the intercage jump processes are interrupted and fast localized motions with very low activation energies are present. By ^{7}Li NMR relaxometry their observation is now fully supported. The calculations by Pecher *et al.* point in the same direction.[40] As an example, De Klerk *et al.* report an activation energy as low as 0.05 eV for the doublet jump process in Li_6PS_5I.[50]

Besides these peculiarities for Li_6PS_5Cl and Li_6PS_5I, the complex ion dynamics in Li-bearing argyrodites with anion disorder is reflected in the distribution of activation energies. Table 6 summarises the activation energies obtained by the different methods applied. Depending on the length-scale and time-scale to which the specific method is sensitive quite different activation energies can be probed. Such a result is typical for ionic conductors whose charge carriers are exposed to an irregularly shaped energy landscape that gives rise to highly correlated forward and backward motions or fast (local) dynamics on the angstrom length scale.

4 Summary and conclusion

We studied the Li ion dynamics in argyrodite-type Li_6PS_5X (X: Cl, Br, I) by a wide range of complementary techniques with a special focus on conductivity spectroscopy and nuclear magnetic relaxation. The latter technique is able to probe short-range as well as long-range bulk ion dynamics. The analysis of electric modulus data also helped us to shed light on the bulk ion dynamics. In all compounds, even in those where two different halogen atoms were used to replace a sulfur anion per formula unit, complex ion dynamics is found. Heterogenous Li ion transport is traced back to the fact of an irregularly shaped potential landscape that the ions are exposed to during diffusion. The vacancy-rich Li sublattice offers a range of hopping barriers between the Li sites involved in the overall ionic transport. Depending on the method applied to study the hopping processes, Li ion translational motions on quite different time scales and lengths scales are probed. This circumstance results in activation energies ranging from 0.08 eV to values as high as 0.48 eV.

Anion disorder in Li_6PS_5Br and Li_6PS_5Cl, as verified by X-ray powder diffraction measurements, boosts the ion dynamics as compared to the parent compound Li_7PS_6. The halogen anions are clearly distributed over the crystallographic sites 4a and 4d. Li_6PS_5Br reveals the lowest activation energies and the bulk ion conductivities follow a single Arrhenius line. Deviations from this behaviour are seen for Li_6PS_5Cl and Li_6PS_5I. For Li_6PS_5Cl an additional dynamic process shows up at higher T, which is also seen in ^{7}Li spin-lock NMR spectroscopy. This process leads to a relatively high mean activation energy in σ_{DC} characterising the overall ion transport.

Most importantly, also for the poor ionic conductor Li_6PS_5I our NMR relaxation measurements reveal very fast Li ion dynamics on a local to medium-range length scale. Obviously, the ions have access to the same, rapid exchange processes as in Li_6PS_5Br but long-range transport is switched off. In the spirit of De Klerk and co-workers we think that the ordered anion sublattice, combined with the larger lattice constant, is responsible for this peculiarity. It leads to a heterogeneous potential landscape with low and high hopping barriers. High activation barriers seem to characterize the intercage jumps; these jump processes are, however, necessary to transport the ions over long distances.

Conflicts of interest

There are no conflicts to declare.

Acknowledgements

Financial support by the Deutsche Forschungsgemeinschaft (DFG Research Unit 1277, grant no. WI3600/2-1(4-1) (FOR1277)) as well as by the Austrian Federal Ministry of Science, Research and Economy, and the Austrian National Foundation for Research, Technology and Development (Christian Doppler Laboratory of Lithium Batteries: Ageing Effects, Technology and New Materials) is greatly appreciated. Furthermore, we thank the FFG in the frame of the K project safe battery.

References

1 M. S. Whittingham, *Chem. Rev.*, 2004, **104**, 4271.
2 J. B. Goodenough and Y. Kim, *Chem. Mater.*, 2010, **22**, 587.
3 *Lithium Ion Batteries*, ed. M. Wakihara and O. Yamamoto, Wiley-VCH, Weinheim, 1998.
4 A. S. Aricó, P. Bruce, B. Scrosati, J.-M. Tarascon and W. V. Schalkwijc, *Nat. Mater.*, 2005, **4**, 366.
5 P. G. Bruce, B. Scrosati and J.-M. Tarascon, *Angew. Chem., Int. Ed.*, 2008, **47**, 2930.
6 B. L. Ellis and L. F. Nazar, *Curr. Opin. Solid State Mater. Sci.*, 2012, **16**, 168.
7 V. Etacheri, R. Marom, R. Elazari, G. Salitra and D. Aurbach, *Energy Environ. Sci.*, 2011, **4**, 3243–3262.
8 V. Thangadurai, S. Narayanan and D. Pinzaru, *Chem. Soc. Rev.*, 2014, **43**, 4714–4727.
9 J. C. Bachman, S. Muy, A. Grimaud, H.-H. Chang, N. Pour, S. F. Lux, O. Paschos, F. Maglia, S. Lupart, P. Lamp, L. Giordano and Y. Shao-Horn, *Chem. Rev.*, 2016, **116**, 140–162.
10 Z. Zhang, Y. Shao, B. Lotsch, Y.-S. Hu, H. Li, J. Janek, L. F. Nazar, C.-W. Nan, J. Maier, M. Armand and L. Chen, *Energy Environ. Sci.*, 2018, **11**, 1945–1976.
11 M. Uitz, V. Epp, P. Bottke and M. Wilkening, *J. Electroceram.*, 2017, **38**, 142–156.
12 A. Hayashi and M. Tatsumisago, *Electron. Mater. Lett.*, 2012, **8**, 199.
13 N. Kamaya, K. Homma, Y. Yamakawa, M. Hirayama, R. Kanno, M. Yonemura, T. Kamiyama, Y. Kato, S. Hama, K. Kawamoto and A. Mitsui, *Nat. Mater.*, 2011, **10**, 682–686.
14 S. Hori, T. Saito, K. Suzuki, M. Hirayama, A. Mitsui, M. Yonemura, H. Iba and R. Kanno, *Nat. Energy*, 2016, **1**, 16303.
15 V. Epp, O. Gün, H.-J. Deiseroth and M. Wilkening, *J. Phys. Chem. Lett.*, 2013, **4**, 2118–2123.
16 D. Brinkmann, *Prog. Nucl. Magn. Reson. Spectrosc.*, 1992, **24**, 527.
17 P. Knauth, *Solid State Ionics*, 2009, **180**, 911.
18 J. Fergus, *J. Power Sources*, 2010, **195**, 4554–4569.
19 C. Julien and G. A. Nazri, *Solid State Batteries: Materials, Design and Optimization*, Kluwer Academic, Boston, 1994.
20 S. Jacke, J. Song, L. Dimesso, J. Brötz, D. Becker and W. Jägermann, *J. Power Sources*, 2011, **196**, 6911–6914.
21 S. Wang, L. Ben, H. Li and L. Chen, *Solid State Ionics*, 2014, **268**, 110–116.
22 R. Murugan, V. Thangadurai and W. Weppner, *Angew. Chem., Int. Ed.*, 2007, **46**, 7778.
23 S. Narayanan, V. Epp, M. Wilkening and V. Thangadurai, *RSC Adv.*, 2012, **2**, 2553.
24 V. Epp, Q. Ma, E.-M. Hammer, F. Tietz and M. Wilkening, *Phys. Chem. Chem. Phys.*, 2015, **17**, 32115–32121.
25 H. Buschmann, J. Dölle, S. Berendts, A. Kuhn, P. Bottke, M. Wilkening, P. Heitjans, A. Senyshyn, H. Ehrenberg, A. Lotnyk, V. Duppel, L. Kienle and J. Janek, *Phys. Chem. Chem. Phys.*, 2011, **13**, 19378.
26 B. Stanje, D. Rettenwander, S. Breuer, M. Uitz, S. Berendts, M. Lerch, R. Uecker, G. Redhammer, I. Hanzu and M. Wilkening, *Ann. Phys.*, 2017, **529**, 1700140.
27 S. Breuer, D. Prutsch, Q. Ma, V. Epp, F. Preishuber-Pflügl, F. Tietz and M. Wilkening, *J. Mater. Chem. A*, 2015, **3**, 21343–21350.

28 S. Lunghammer, Q. Ma, D. Rettenwander, I. Hanzu, F. Tietz and H. Wilkening, *Chem. Phys. Lett.*, 2018, **701**, 147–150.

29 P. Bron, S. Johansson, K. Zick, J. Schmedt auf der Günne, S. Dehnen and B. Roling, *J. Am. Chem. Soc.*, 2013, **135**, 15694–15697.

30 S. Wenzel, S. Randau, T. Leichtweiß, D. A. Weber, J. Sann, W. G. Zeier and J. Janek, *Chem. Mater.*, 2016, **28**, 2400–2407.

31 H.-J. Deiseroth, S.-T. Kong, H. Eckert, J. Vannahme, C. Reiner, T. Zaiss and M. Schlosser, *Angew. Chem., Int. Ed.*, 2008, **47**, 755–758.

32 S. Boulineau, M. Courty, J.-M. Tarascon and V. Viallet, *Solid State Ionics*, 2012, **221**, 1–5.

33 S. Boulineau, J.-M. Tarascon, J.-B. Leriche and V. Viallet, *Solid State Ionics*, 2013, **242**, 45–48.

34 M. A. Kraft, S. P. Culver, M. Calderon, F. Böcher, T. Krauskopf, A. Senyshyn, C. Dietrich, A. Zevalkink, J. Janek and W. G. Zeier, *J. Am. Chem. Soc.*, 2017, **139**, 10909–10918.

35 R. P. Rao and S. Adams, *Phys. Status Solidi*, 2011, **208**, 1804–1807.

36 P. R. Rayavarapu, N. Sharma, V. K. Peterson and S. Adams, *J. Solid State Electrochem.*, 2012, **16**, 1807–1813.

37 H. M. Chen, C. Maohua and S. Adams, *Phys. Chem. Chem. Phys.*, 2015, **17**, 16494–16506.

38 R. P. Rao, N. Sharma, V. Peterson and S. Adams, *Solid State Ionics*, 2013, **230**, 72–76.

39 H.-J. Deiseroth, J. Maier, K. Weichert, V. Nickel, S.-T. Kong and C. Reiner, *Z. Anorg. Allg. Chem.*, 2011, **637**, 1287–1294.

40 O. Pecher, S.-T. Kong, T. Göbel, V. Nickel, K. Weichert, C. Reiner, H.-J. Deiseroth, J. Maier, F. Haarmann and D. Zahn, *Chem. – Eur. J.*, 2010, **16**, 8347–8354.

41 A. Düvel, B. Ruprecht, P. Heitjans and M. Wilkening, *J. Phys. Chem. C*, 2011, **115**, 23784–23789.

42 S. Breuer and M. Wilkening, *Dalton Trans.*, 2018, **47**, 4105–4117.

43 B. Kozinsky, S. A. Akhade, P. Hirel, A. Hashibon, C. Elsässer, P. Mehta, A. Logeat and U. Eisele, *Phys. Rev. Lett.*, 2016, **116**, 055901.

44 K. E. Kweon, J. B. Varley, P. Shea, N. Adelstein, P. Mehta, T. W. Heo, T. J. Udovic, V. Stavila and B. C. Wood, *Chem. Mater.*, 2017, **29**, 9142–9153.

45 E. Fukushima and S. Roeder, *Experimental Pulse NMR*, Addison-Wesley, Reading, 1981.

46 V. Epp, O. Gün, H.-J. Deiseroth and M. Wilkening, *Phys. Chem. Chem. Phys.*, 2013, **15**, 7123–7132.

47 D. C. Look and I. J. Lowe, *J. Chem. Phys.*, 1966, **44**, 2995.

48 D. C. Ailion and C. P. Slichter, *Phys. Rev.*, 1965, **137**, A235.

49 S.-T. Kong, H.-J. Deiseroth, C. Reiner, Z. Gün, E. Neumann, C. Ritter and D. Zahn, *Chem. – Eur. J.*, 2010, **16**, 2198–2206.

50 N. J. J. de Klerk, I. Roslon and M. Wagemaker, *Chem. Mater.*, 2016, **28**, 7955–7963.

51 F. Preishuber-Pflügl, P. Bottke, V. Pregartner, B. Bitschnau and M. Wilkening, *Phys. Chem. Chem. Phys.*, 2014, **16**, 9580–9590.

52 F. Preishuber-Pflügl and M. Wilkening, *Dalton Trans.*, 2016, **45**, 8675–8687.

53 F. Preishuber-Pflügl and M. Wilkening, *Dalton Trans.*, 2014, **43**, 9901–9908.

54 M. Wilkening, A. Düvel, F. Preishuber-Pflügl, K. Silva, S. Breuer, V. Šepelák and P. Heitjans, *Z. Kristallogr. - Cryst. Mater.*, 2016, **232**, 107–127.

55 D. L. Sidebottom, *Rev. Mod. Phys.*, 2009, **81**, 999.

56 R. Metselaar and G. Oversluizen, *J. Solid State Chem.*, 1984, **55**, 320–326.

57 J. T. S. Irvine, D. C. Sinclair and A. R. West, *Adv. Mater.*, 1990, **2**, 132–138.

58 K. L. Ngai, *Relaxation and Diffusion in Complex Systems*, Springer, New York, 2011.

59 K. L. Ngai, G. N. Greaves and C. T. Moynihan, *Phys. Rev. Lett.*, 1998, **80**, 1018.

60 R. Winter, K. Siegmund and P. Heitjans, *J. Non-Cryst. Solids*, 1997, **212**, 215–224.

61 M. Wilkening and P. Heitjans, *Chem. Phys. Chem.*, 2012, **13**, 53–65.

62 P. Heitjans, A. Schirmer and S. Indris, in *Diffusion in Condensed Matter*, ed. P. Heitjans and J. Kärger, Springer, 2005, ch. 9, p. 367.

63 V. Epp, C. Brüning, M. Binnewies, P. Heitjans and M. Wilkening, *Z. Phys. Chem.*, 2012, **226**, 513.

64 M. Wilkening, A. Kuhn and P. Heitjans, *Phys. Rev. B: Condens. Matter Mater. Phys.*, 2008, **78**, 054303.

65 A. Kuhn, S. Narayanan, L. Spencer, G. Goward, V. Thangadurai and M. Wilkening, *Phys. Rev. B: Condens. Matter Mater. Phys.*, 2011, **83**, 094302.

66 P. Heitjans and M. Wilkening, *Defect Diffus. Forum*, 2009, **283–286**, 705.

67 M. Wilkening and P. Heitjans, *Phys. Rev. B: Condens. Matter Mater. Phys.*, 2008, **77**, 024311.

68 M. Wilkening, W. Küchler and P. Heitjans, *Phys. Rev. Lett.*, 2006, **97**, 065901.

69 N. Bloembergen, E. M. Purcell and R. V. Pound, *Phys. Rev.*, 1948, **73**, 679–712.

70 W. Küchler, P. Heitjans, A. Payer and R. Schöllhorn, *Solid State Ionics*, 1994, **70/71**, 434.

71 M. Meyer, P. Maass and A. Bunde, *Phys. Rev. Lett.*, 1993, **71**, 573–576.

72 A. Kuhn, P. Sreeraj, R. Pöttgen, H.-D. Wiemhöfer, M. Wilkening and P. Heitjans, *J. Am. Chem. Soc.*, 2011, **133**, 11018–11021.

73 A. Kuhn, S. Narayanan, L. Spencer, G. Goward, V. Thangadurai and M. Wilkening, *Phys. Rev. B: Condens. Matter Mater. Phys.*, 2011, **83**, 094302.

74 T. M. Kirschgen, M. D. Zeidler, B. Geil and F. Fujara, *Phys. Chem. Chem. Phys.*, 2003, **5**, 5243–5246.

75 R. Bertermann and W. Müller-Warmuth, *Z. Naturforsch., A: Phys. Sci.*, 1998, **53**, 863–873.

76 E. Göbel, W. Müller-Warmuth, H. Olyschläger and H. Dutz, *J. Magn. Reson.*, 1979, **36**, 371–387.

77 C. Yu, S. Ganapathy, E. R. H. van Eck, L. van Eijck, S. Basak, Y. Liu, L. Zhang, H. Zandbergen and M. Wagemaker, *J. Mater. Chem. A*, 2017, **5**, 21178–21188.

78 K. Hayamizu, S. Tsuzuki and S. Seki, *Magn. Reson. Chem.*, 2011, **49**, 6–8.

79 M. Grüne, H. Meierkord, W. Müller-Warmuth, P. Z. Hebel, B. Krebs and M. Wulff, *Ber. Busenges. Phys. Chem.*, 1989, **93**, 1313–1317.

80 M. Wilkening, D. Bork, S. Indris and P. Heitjans, *Phys. Chem. Chem. Phys.*, 2002, **4**, 3246–3251.

81 A. Abragam, *The principles of nuclear magnetism*, Oxford University Press, 1999.

82 J. R. Hendrickson and P. J. Bray, *J. Magn. Reson.*, 1973, **9**, 341–357.

83 J. R. Hendrickson and P. J. Bray, *J. Chem. Phys.*, 1974, **61**, 2754–2764.

84 H. Mehrer, *Diffusion in Solids: Fundamentals, Methods, Materials, Diffusion-Controlled Processes*, Springer, Berlin, 2007.